

# **Novel Solar Sail Mission Concepts for High-Latitude Earth and Lunar Observation<sup>1</sup>**

Jeannette Heiligers<sup>2</sup>  
*Delft University of Technology, 2629 HS Delft, the Netherlands*  
*University of Colorado, Boulder, CO 80309, USA*

Jeffrey S. Parker<sup>3</sup>  
*University of Colorado, Boulder, CO 80309, USA*

*and*

Malcolm Macdonald<sup>4</sup>  
*University of Strathclyde, Glasgow G1 1XJ, Glasgow, United Kingdom*

**Solar sail periodic orbits in the Earth-Moon circular restricted three-body problem are proposed for continuous observation of the polar regions of the Earth and the Moon. The existence of families of solar sail periodic orbits in the Earth-Moon system has previously been demonstrated by the authors and is expanded by introducing additional orbit families. Orbits for near-term solar sail technology originate by maintaining the solar sail at a constant attitude with respect to the Sun such that mission operations are greatly simplified. The results of this investigation include a constellation of two solar sail L<sub>2</sub>-vertical Lyapunov orbits that achieves continuous observation of both the lunar South Pole and the center of the Aitken Basin at a minimum elevation of 15 deg. At Earth, a set of two, clover-shaped orbits can provide continuous coverage of one of the Earth's poles at a**

---

<sup>1</sup> Part of this work was presented at the 2016 AIAA/AAS Astrodynamics Specialist Conference, Long Beach, California, September 2016

<sup>2</sup> Marie Curie Research Fellow, Faculty of Aerospace Engineering, Kluyverweg 1, and Colorado Center for Astrodynamics Research, AIAA Member.

<sup>3</sup> Assistant Professor, Colorado Center for Astrodynamics Research, AIAA Senior Member

<sup>4</sup> Reader, Strathclyde Space Institute, AIAA Associate Fellow.

**minimum elevation of 20 deg. Results generated in the Earth-Moon circular restricted three-body model are easily transitioned to one that includes eccentricity effects and demonstrates that the orbits are feasible in realistic regimes.**

## **I. Introduction**

The successes of JAXA's IKAROS (2010), NASA's NanoSail-D2 (2010), and The Planetary Society's LightSail-1 (2015) missions have renewed interest in solar sailing. Research in the field is flourishing and more initiatives are scheduled for the future (e.g., NEA Scout (NASA) [1]). The unique feature of not relying on an onboard reaction mass makes solar sailing the preferred option for a range of mission applications [2, 3]. Key mission concepts include: precessing an elliptical Earth-centered orbit for long residence times in the Earth's magnetotail (i.e., the GeoSail mission concept) [4-7], hovering along the Sun-Earth line sunward of the  $L_1$  point for increased warning times for space weather events (i.e., the GeoStorm mission concept) [8, 9], using a sail to achieve a solar polar orbiting probe for high-latitude and close proximity observations of the Sun [5, 10], as well as more far-term concepts, such as the interstellar heliopause probe where a close approach of the Sun is used for a photon-gravity assist, which allows a rapid transit through the Solar System without the need for a heavy-lift launch vehicle or a long sequence of gravity assists [11].

The purpose of the current investigation is to add to this extensive list of potential solar sail applications by focusing on the sail's potential for high-latitude observation of the Earth and the Moon. Continuous observation of terrestrial high-latitudes will be crucial for on-going studies of global climate change and also to support telecommunications, weather forecasting, and ship navigation for the exploration and sustainable development of these regions. The northern polar region is of significant interest as it is projected to hold 30 percent of the Earth's undiscovered gas and 13 percent of the Earth's undiscovered oil [12]. In addition, with northern sea routes opening up from melting ice caps, an increase in shipping activity can be expected. Finally, continuous observation of the high-latitudes of the Earth is also important for space weather monitoring and forecasting activities. For example, a continuous view of the *entire* aurora oval allows observations of the direct response of the magnetosphere to changes in the solar wind, which is critical to understanding the solar wind-magnetosphere coupling. This monitoring will also enable the detection and imaging of rarely observed phenomena such as transpolar arcs and cusp spots [13] to further the understanding of the causes for and relationships between these phenomena. Regarding the Moon, the permanently shadowed craters on the lunar South Pole, especially the Shackleton Crater, are of significant scientific interest and could be the future destination of a permanently occupied lunar base, especially as the lunar South Pole exhibits so-called "peaks of eternal light" providing

near-permanent sunlight conditions and therefore access to power. Both objectives require continuous observation capabilities of the lunar South Pole and, in case of a lunar base, also continuous communication with Earth. This investigation establishes these continuous links with high-latitude regions through the use of solar sail periodic orbits in the Earth-Moon three-body system. These orbits are generated by differential correction techniques and by perturbing classical libration point orbits such as Lyapunov, halo, vertical Lyapunov and distant retrograde orbits with a solar sail induced acceleration. As such, entirely new families of orbits, parameterized by the sail's acceleration, are established in the Earth-Moon system [14, 15]. Different types of families can be created based on the steering law assumed for the solar sail. In this study a simple law, either Sun-facing or one where the sail is pitched at a constant angle with respect to the Sun-direction, is assumed, endeavoring to minimize mission operations. However, the approach described in the paper and the tools and techniques employed can be applied to a variety of steering laws, as long as the steering law is symmetric with respect to the direction of sunlight and periodic with the Sun's orbital motion around the Earth-Moon system.

Not only does this study add an additional family of solar sail orbits to previous work [14, 15], it also incorporates the effects of higher-fidelity dynamics on the existence and properties of the solar sail periodic orbits. While previous work by the authors assumed that the ecliptic and Earth-Moon planes coincide and neglected the solar gravity and Earth and lunar eccentricities, this investigation accounts for these effects, providing realistic solar sail trajectories by expanding the differential correction technique to a multiple shooting differential correction method.

## II. Solar sail dynamics

Initial investigations into the families of solar sail periodic orbits in the Earth-Moon system are conducted within the framework of the circular restricted three-body problem (CR3BP) [16] and are extended to a higher-fidelity dynamical model in Section V. To describe the solar sail dynamics, the synodic reference frame appearing in Figure 1a is used along with the traditional system of canonical units, where the Earth-Moon distance, the frame's angular velocity,  $\omega$ , and the Earth-Moon system mass are normalized to unity. Then, one sidereal lunar month is  $2\pi$  and with the mass ratio  $\mu = m_2 / (m_1 + m_2)$ , the locations of the Earth and Moon along the  $x$ -axis become  $-\mu$  and  $1 - \mu$ , respectively. Following Reference [2], the solar sail dynamics are governed by

$$\ddot{\mathbf{r}} + 2\boldsymbol{\omega} \times \dot{\mathbf{r}} = \mathbf{a}_s - \nabla U. \quad (1)$$

In Eq. (1),  $\mathbf{r} = [x \ y \ z]^T$  is the solar sail dimensionless position vector with respect to the Earth-Moon barycenter and with coordinates in the synodic frame of Figure 1a,  $\boldsymbol{\omega} = \omega \hat{\mathbf{z}}$  is the synodic frame's angular velocity vector and  $U = -\frac{1}{2}(x^2 + y^2) - ([1-\mu]/r_1 + \mu/r_2)$  is the effective potential with the Earth-sail and Moon-sail vectors defined as  $\mathbf{r}_1 = [x + \mu \ y \ z]^T$  and  $\mathbf{r}_2 = [x - (1-\mu) \ y \ z]^T$ , respectively.

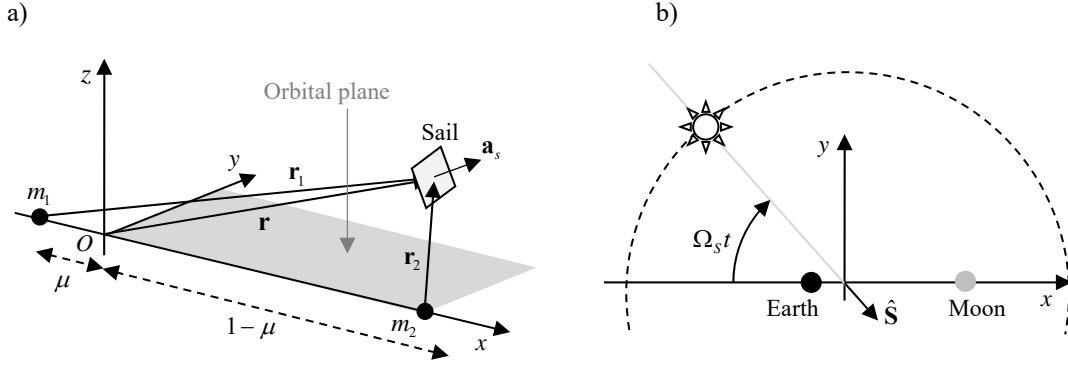


**Figure 1a) Solar sail circular restricted three-body reference frame. b) Orbital motion of Sun in the reference frame of subplot a).**

The term that differentiates Eq. (1) from the classical CR3BP dynamical system is the solar sail induced acceleration,  $\mathbf{a}_s$ . To define this acceleration it is important to note that, when considering the synodic reference frame of Figure 1a, the Sun “orbits” around the Earth-Moon system once per synodic lunar period, as illustrated in Figure 1b, and therefore the direction of the photons with respect to the frame changes over time, making the dynamics in Eq. (1) time dependent. In particular, the Sun-direction,  $\hat{\mathbf{S}}$ , can be described as:

$$\hat{\mathbf{S}}(t) = \begin{bmatrix} \cos(\Omega_s t) \\ -\sin(\Omega_s t) \\ 0 \end{bmatrix} = R_z(-\Omega_s t) \begin{bmatrix} 1 \\ 0 \\ 0 \end{bmatrix} \quad (2)$$

with  $\Omega_s = 0.9252$  the Sun's dimensionless orbital angular rate ( $2.4509 \times 10^{-6}$  rad/s in dimensional form),  $t$  the dimensionless time, and  $R_z(-\Omega_s t)$  the rotation matrix around the  $z$ -axis over an angle  $-\Omega_s t$ . Note that the small offset between the Earth-Moon and ecliptic planes of approximately 5 deg as well as the orbital eccentricity of both the Earth and Moon, which all have an effect on the value for  $\Omega_s$ , is neglected in this formulation. However, models accounting for these effects are presented in Section V. It is furthermore important to note that this paper adopts an ideal solar sail model, whereby the solar photons are specularly reflected and the solar radiation pressure force acts perpendicular to the solar sail membrane, along the sail

normal vector  $\hat{\mathbf{n}}$  [2, 3]. Note that a small tangential force component exists with more realistic sail reflectance models, but previous analyses have shown that this component has only a small effect on the solar sail induced acceleration magnitude and direction [9]. Therefore, when neglecting this tangential component, the solar sail induced acceleration is given by

$$\mathbf{a}_s = a_{0,EM} (\hat{\mathbf{S}}(t) \cdot \hat{\mathbf{n}})^2 \hat{\mathbf{n}}. \quad (3)$$

In Eq. (3) the magnitude of the acceleration,  $a_{0,EM} (\hat{\mathbf{S}}(t) \cdot \hat{\mathbf{n}})^2$ , is assumed to be independent of the sail's location in the Earth-Moon system, i.e., the Sun-sail distance is assumed to be constant throughout the Earth-Moon system at 1 astronomical unit (au). Furthermore, the term  $(\hat{\mathbf{S}}(t) \cdot \hat{\mathbf{n}})^2$  accounts for the sail's reduced effective area and achievable solar sail induced acceleration when pitching the sail away from the Sun-direction.

In this investigation, two different types of sail orientations will be considered. The first scenario is a Sun-facing steering law in which the sail orientation follows the direction of sunlight over time, exposing its full membrane to the Sun at all times, see Figure 2a. The solar sail normal vector *with respect to the Sun-vector*,  $\mathbf{n}_s$ , then equals  $\mathbf{n}_s = [1 \ 0 \ 0]^T$ , from which the solar sail normal vector in the synodic reference frame of Figure 1a can be retrieved through  $\hat{\mathbf{n}} = R_z(-\Omega_s t) \hat{\mathbf{n}}_s$ , reducing Eq. (3) to

$$\mathbf{a}_s = a_{0,EM} R_z(-\Omega_s t) \hat{\mathbf{n}}_s = a_{0,EM} R_z(-\Omega_s t) \begin{bmatrix} 1 \\ 0 \\ 0 \end{bmatrix} = a_{0,EM} \hat{\mathbf{S}}(t). \quad (4)$$

Note that for such a Sun-facing steering law, the tangential force component of more realistic solar sail reflectance models does not play a role because the effect of non-ideal properties of the sail would only be a reduction in the acceleration magnitude,  $a_{0,EM}$  [9]. The second scenario pitches the sail in the out-of-plane direction at an angle  $\gamma$  with respect to the Sun-direction, see Figure 2b. The solar sail normal vector *with respect to the Sun-vector*,  $\mathbf{n}_s$ , then equals  $\mathbf{n}_s = R_y(-\gamma) [1 \ 0 \ 0]^T$ , again resulting in a solar sail normal vector in the synodic reference frame of  $\hat{\mathbf{n}} = R_z(-\Omega_s t) \hat{\mathbf{n}}_s$  and reducing Eq. (3) to:

$$\mathbf{a}_s = a_{0,EM} \cos^2 \gamma R_z(-\Omega_s t) \hat{\mathbf{n}}_s = a_{0,EM} \cos^2 \gamma R_z(-\Omega_s t) R_y(-\gamma) \begin{bmatrix} 1 \\ 0 \\ 0 \end{bmatrix} = a_{0,EM} \cos^2 \gamma \begin{bmatrix} \cos \gamma \cos \Omega_s t \\ -\cos \gamma \sin \Omega_s t \\ \sin \gamma \end{bmatrix}, \quad (5)$$

where the term  $\cos^2 \gamma$  comes from the term  $(\hat{\mathbf{S}}(t) \cdot \hat{\mathbf{n}})^2$  in Eq. (3). Note that both steering laws in Eqs. (4) and (5) can, hypothetically, be achieved passively through a correct offset between the spacecraft's center-of-pressure and center-of-mass.

The variable  $a_{0,EM}$  is commonly called the characteristic acceleration, i.e., the acceleration that an ideal solar sail generates when facing the Sun at 1 au [2]. A common value for this acceleration, based on near-term solar sail technology, is  $0.3 \text{ mm/s}^2$  [5, 9], which translates into a dimensionless value of approximately  $a_{0,EM} = 0.1$ . This study does not consider characteristic accelerations beyond this value and shows only what is achievable with near-term solar sail technology.

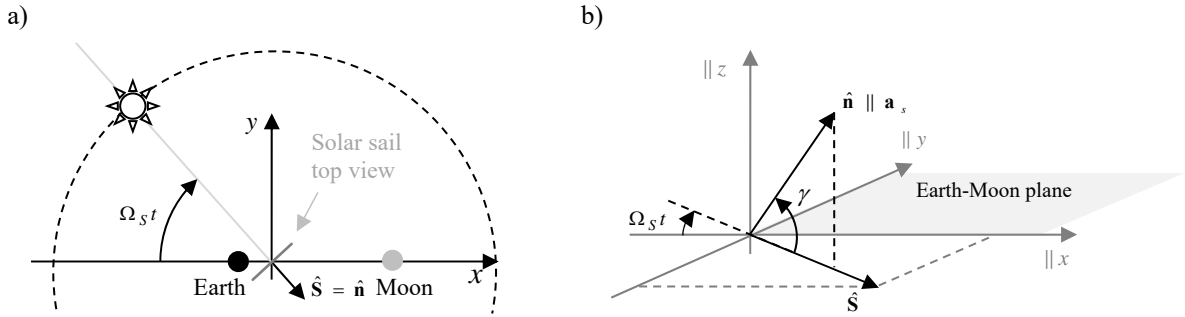


**Figure 2a) Passive Sun-facing solar sail steering law b) Out-of-plane solar sail steering law.**

### III. Solar sail periodic orbits

To find solar sail periodic orbits obeying the dynamics of Eq. (1), a classical differential corrector scheme is applied [15, 17] that relies on the use of a state transition matrix to iteratively solve for the initial conditions that lead to periodic motion. Furthermore, the eigenvalues of the state transition matrix supply the linear stability properties of these orbits. However, the differential corrector scheme used here differs from the one presented in Reference [17] in two aspects: first, as the Sun direction,  $\hat{\mathbf{S}}(t)$ , continuously changes, the system is time dependent and orbits are repeatable over time (and thus periodic) only if the period of the orbit coincides with the Sun's orbital motion around the Earth-Moon system. The period of any solar sail periodic orbit in the Earth-Moon system thus needs to equal  $2\pi/\Omega_S$  or a multiple thereof. The authors have previously adapted the differential corrector scheme in Reference [17] to include a constraint such that the period is indeed driven towards a value of  $2\pi/\Omega_S$  [15]. This constraint also provides an additional equation to solve for one of the unknown initial states, leading to the second difference: while the differential corrector scheme for classical

orbits requires one of the unknown initial states to be fixed, the addition of the periodicity constraint allows all initial states to be free. This feature is important as it cannot be known *a priori* where (i.e., for which value of any of the initial states) solar sail periodic orbits exist in the Earth-Moon system. For details on the adapted differential corrector scheme, the reader is referred to Reference [15].

To seed the differential corrector, a continuation scheme is applied where a classical periodic orbit is employed as the initial guess for a very small value for the solar sail characteristic acceleration; the result of that simulation is used as initial guess for a slightly larger solar sail characteristic acceleration value. By continuing this process up to a maximum value for the characteristic acceleration of  $a_{0,EM} = 0.1$ , families of solar sail periodic orbits in the Earth-Moon system arise for increasing sail performance. Note that the periodic orbit used in the first step of the continuation scheme is chosen from the family of periodic orbits in the classical CR3BP with the period coinciding with  $2\pi / \Omega_s$  or a fraction of it.

Two example families appear in Figure 3 and Figure 5; both will be exploited for high-latitude observation of the Earth and the Moon. The family appearing in Figure 3 is coined the family of clover-shaped orbits after the shape of its projection onto the  $(x, y)$ -plane. These orbits employ the steering law in Eq. (4) and originate via the continuation on the value for  $a_{0,EM}$  (indicated by the grayscale in Figure 3a-d), starting from a classical, highly-elliptical Earth-centered orbit with a period of half the synodic lunar month. As this classical orbit passes through the Earth (see Figure 3c) it is of no practical use; however, adding a solar sail induced acceleration moves this orbit away from the Earth's center. Periodic structure is clearly apparent in the shape of these orbits as observed in a Sun-Earth synodic ("SE-synodic") reference frame, where the  $x$ -axis remains along the Sun-Earth line, the  $z$ -axis is perpendicular to the Earth-Moon orbital plane, and the  $y$ -axis completes the right-handed reference frame. Figure 4 displays two of the orbits, with  $a_{0,EM} = 0.025$  and  $a_{0,EM} = 0.1$ , in this reference frame over a period of 1 year. From Figure 4 it is clear that the orbits appear to resemble highly-elliptic, Sun-synchronous orbits. A close-up inspection of the orbits furthermore shows the effect of the Moon, which tilts the orbits slightly away from the vertical and creates two lobes per orbital period that are slightly offset in the anti-Sun direction.

A plot of the stability of the clover-shaped orbit family as a function of the characteristic acceleration appears in Figure 3e and is represented by the value of the largest eigenvalue,  $\|\lambda\|_{\max}$ , of the monodromy matrix. An orbit is considered to be stable if all six eigenvalues lie on the unit circle in the complex plane, i.e.,

$\|\lambda\|_{\max} = 1$ . If the norm of any of the eigenvalues is larger than one, the orbit is unstable, with larger norm values indicating greater instability. Figure 3e indicates that for the solar sail characteristic acceleration magnitudes considered in this study ( $a_{0,EM} \leq 0.1$ ) the orbits are slightly unstable, but that they are stable for larger acceleration magnitudes.

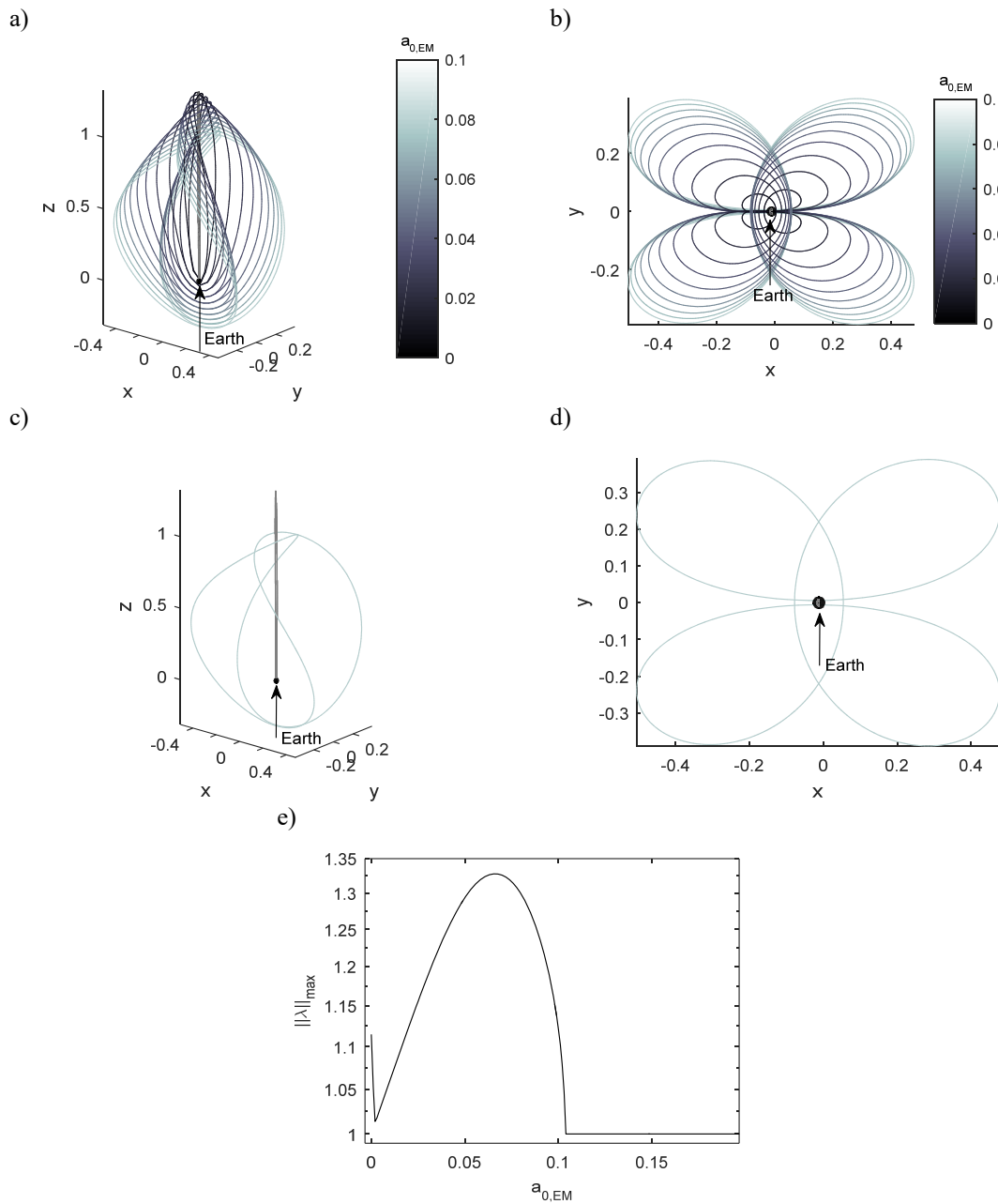


**Figure 3** Solar sail Earth-centered clover-shaped orbits. a,b) Family of orbits. c,d) Orbits for  $a_{0,EM} = 0$  (black) and  $a_{0,EM} = 0.1$  (gray). e) Measure of linear stability.

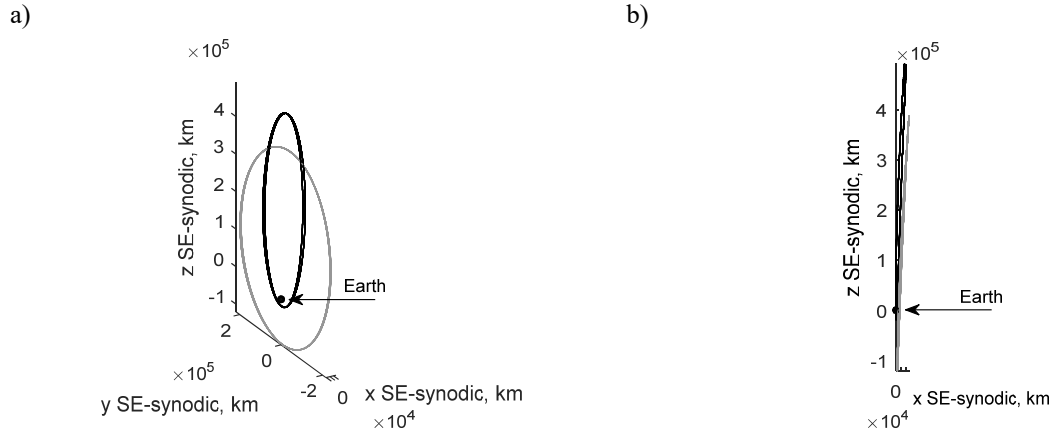


**Figure 4 Solar sail Earth-centered clover-shaped orbits with  $a_{0,EM} = 0.025$  (black) and  $a_{0,EM} = 0.1$  (gray) in Sun-Earth synodic frame.**

The second family in Figure 5 is an example of a family of solar sail vertical Lyapunov orbits at the  $L_2$  point. This family employs the steering law in Eq. (5), with  $\gamma = -35.26$  deg, in a continuation in  $a_{0,EM}$  starting from a classical vertical Lyapunov orbit ( $a_{0,EM} = 0$ ) with a period of two-thirds of the synodic lunar month and increasing the solar sail characteristic acceleration to a maximum value of  $a_{0,EM} = 0.1$ . The value for  $\gamma$  of  $-35.26$  deg is selected because it gives the maximum out-of-plane acceleration component [2] and the minus sign ensures that the acceleration is directed below the Earth-Moon plane, which is important when investigating these orbits for coverage of the southern hemisphere of the Moon (see Section IV.B). Through the use of this steering law, the orbits are slightly displaced in the out-of-plane direction, pulling them below the lunar South Pole. Although all solar sail vertical Lyapunov orbits are highly unstable, see Figure 5g, the solar sail does have a small stabilizing effect as the maximum eigenvalue norm decreases (up to an order of magnitude) for increasing values for  $a_{0,EM}$ . Note that the stability of these orbits may be further improved by employing the sail to correct and control for orbital errors and perturbations. Finally, note that, because the period of these orbits equals two synodic lunar months and the orbits are symmetric in the  $(x, z)$ -plane, at time  $t = 0$  the spacecraft can be placed at either of the two most out-of-plane positions, i.e., either above or below the Earth-Moon plane.

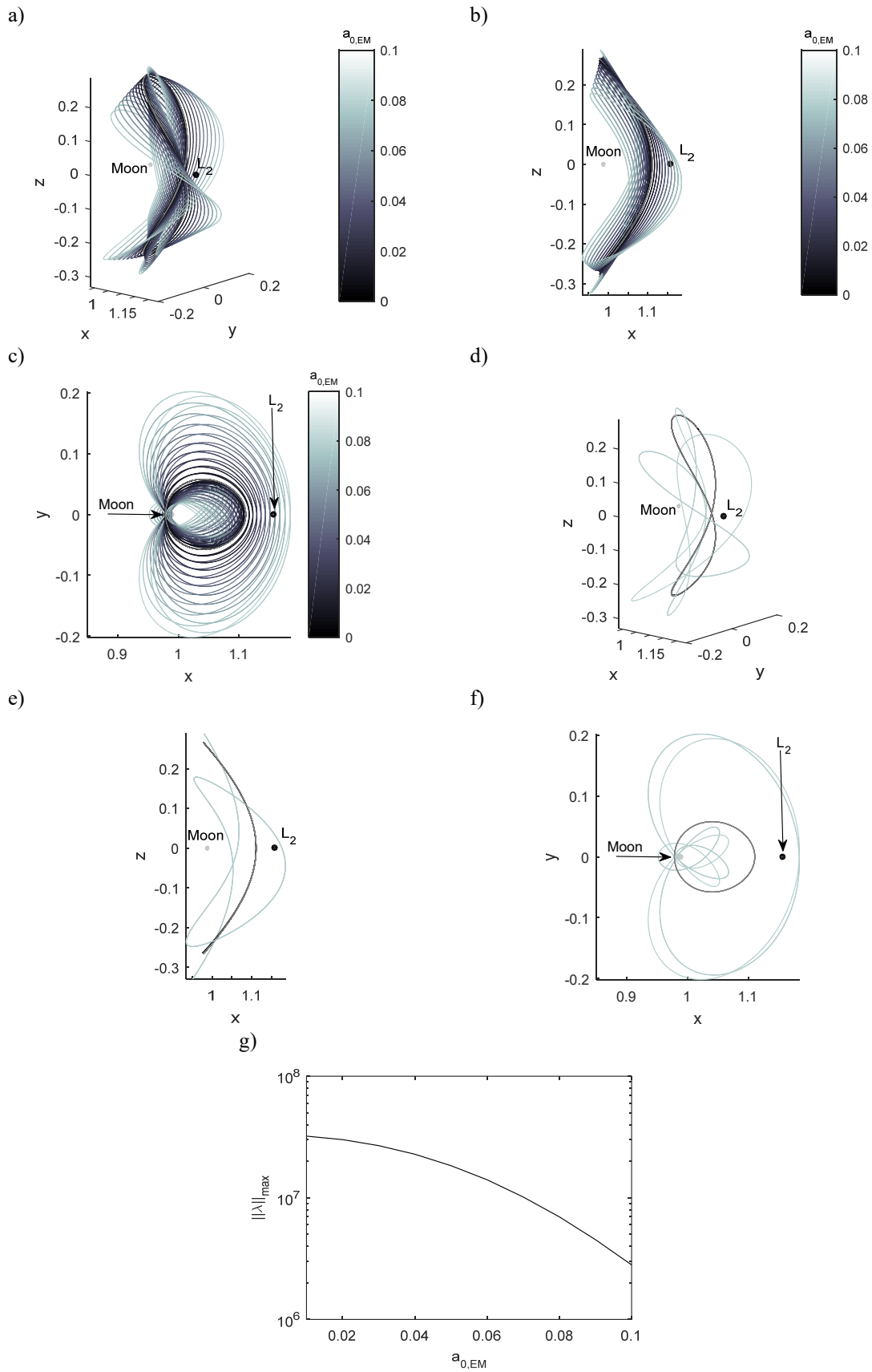


**Figure 5** Solar sail  $L_2$  vertical Lyapunov orbits. a,b,c) Family of orbits. d,e,f) Orbits for  $a_{0,EM} = 0$  (black) and  $a_{0,EM} = 0.1$  (gray). g) Measure of linear stability.

## IV. High-latitude observation analyses

A subset of the orbits presented in Figure 3 and Figure 5 can achieve near-continuous observation of the high-latitudes of the Earth and the Moon. This is demonstrated by computing the spacecraft's elevation,  $\varepsilon$ , over time at different locations on the Earth or the Moon. The metric used is the amount of time that the spacecraft is above a minimum elevation,  $\varepsilon \geq \varepsilon_{\text{lim}}$ , and is expressed as the percentage coverage, i.e., the percentage of time over a full orbital period or a full year that the condition  $\varepsilon \geq \varepsilon_{\text{lim}}$  is satisfied at a particular location or latitude of the Earth or the Moon. Note that the condition  $\varepsilon \geq \varepsilon_{\text{lim}}$  must be evaluated over a full year for the use of the clover-shaped orbits for observation of the Earth due to the seasonal variation of the Earth's polar axis with respect to the Earth-Moon plane. Finally, besides the elevation angle, the range from the ground station is also important and will therefore be assessed for each constellation.

### A. Clover-shaped orbits for Earth observation

Observation of the high-latitudes of the Earth are regularly achieved with satellites in low-altitude, high-inclination orbits such as the ICESat-1 (NASA, 2003 – 2010) and Cryosat-2 (ESA, 2010 – ongoing) missions. Although they enable high spatial resolution observations, the low-altitude of the polar orbits restricts spacecraft to observe only narrow swaths of the polar regions throughout each passage. For example, CryoSat-2 repeats its ground track only after 369 days, with a sub-cycle of 33 days only after which uniform coverage of the polar regions is obtained. Higher temporal resolution is achieved by Molniya orbits, but satisfactory coverage of the polar caps or high-latitude regions is not always achieved. In addition to these traditional concepts, a range of other concepts have been proposed for high-latitude observation, including Taranis orbits [18], pole-sitter orbits [19], solar sail displaced equilibria [20], and eight-shaped orbits [21] in the Sun-Earth system, all providing different trade-offs between resolution of the observations (i.e., distance from Earth), number of spacecraft required for continuous coverage, and required propulsion technology (if any). The current work complements these concepts with the capabilities provided by the clover-shaped orbits appearing in Figure 3. These orbits are closer to Earth than previously proposed solar sail concepts, such as the pole-sitter orbits and displaced equilibria, and require fewer satellites for continuous coverage than constellations in low-altitude orbits.

As mentioned, the percentage of time that the condition  $\varepsilon \geq \varepsilon_{\text{lim}}$  is satisfied is used as the metric to express the high-latitude coverage from the clover-shaped orbits. It is clear from the orbital plots appearing in Figure 3 that one spacecraft cannot provide continuous coverage of these high-latitudes as it travels below the equatorial

plane for short periods of time. A constellation of two spacecraft ('orbit 1' and 'orbit 2') is therefore required, where one of the orbits ('orbit 2') is mirrored in the  $(x, y)$ -plane. To determine which constellation would perform best, a grid search is performed over a combination of characteristic accelerations for each of the orbits with  $a_{0,EM} = [0.025, 0.03, \dots, 0.1]$ . For each constellation, i.e., for each combination of  $a_{0,EM}$  of orbit 1 and  $a_{0,EM}$  of orbit 2, the temporal coverage with a minimum elevation angle of  $\varepsilon_{lim} = 27$  deg is computed at four locations on Earth: the North Pole, the South Poles, the Arctic circle (latitude band of 66.56083 deg), and the 55 deg latitude band (the latter bands employ an average over a 1 deg mesh in longitude). The value for  $\varepsilon_{lim}$  of 27 deg reflects the elevation of a geostationary spacecraft at a latitude of 55 deg above which the accessibility of geostationary spacecraft for Earth observation applications is not assured. The results of the grid search are presented in Figure 6. The horizontal and vertical axes show the dimensionless acceleration of the sailcraft in the two orbits, where a minimum value of  $a_{0,EM} > 0.025$  is considered to ensure a minimum altitude above the Earth of 10,000 km. The grayscale indicates the percentage of time during a full year that the spacecraft is in view of either of the four locations at the previously mentioned minimum elevation of  $\varepsilon_{lim} = 27$  deg.

Based on the need for continuous coverage of the high-latitudes of the Earth, two constellations are selected from the results in Figure 6. First, 'constellation 1' provides the best coverage of the high latitudes of one of the hemispheres with 99.6 percent temporal coverage of the North Pole, see Table 1. This constellation uses characteristic accelerations of  $a_{0,EM} = 0.025$  for orbit 1 and  $a_{0,EM} = 0.1$  for orbit 2. If some reduction in coverage is allowed, a second constellation can be defined that provides the best overall temporal coverage of the high latitudes of both hemispheres ('constellation 2' with both orbits  $a_{0,EM} = 0.025$  only mirrored in the Earth-Moon plane). In this case, the temporal coverage of the North and South Poles reduces to 96.3 percent. Note that, despite the decrease in temporal coverage, the latter constellation may still be of interest as it allows simultaneous support of both shipping activities in the Arctic region and ongoing research activities on Antarctica. Furthermore, the two polar regions do not respond equally to changes in the solar wind and observation of both the aurora borealis and aurora australis will give insights in interhemispheric asymmetries in energy deposition in the atmosphere [22]. More details for both constellations follow in the next two subsections.

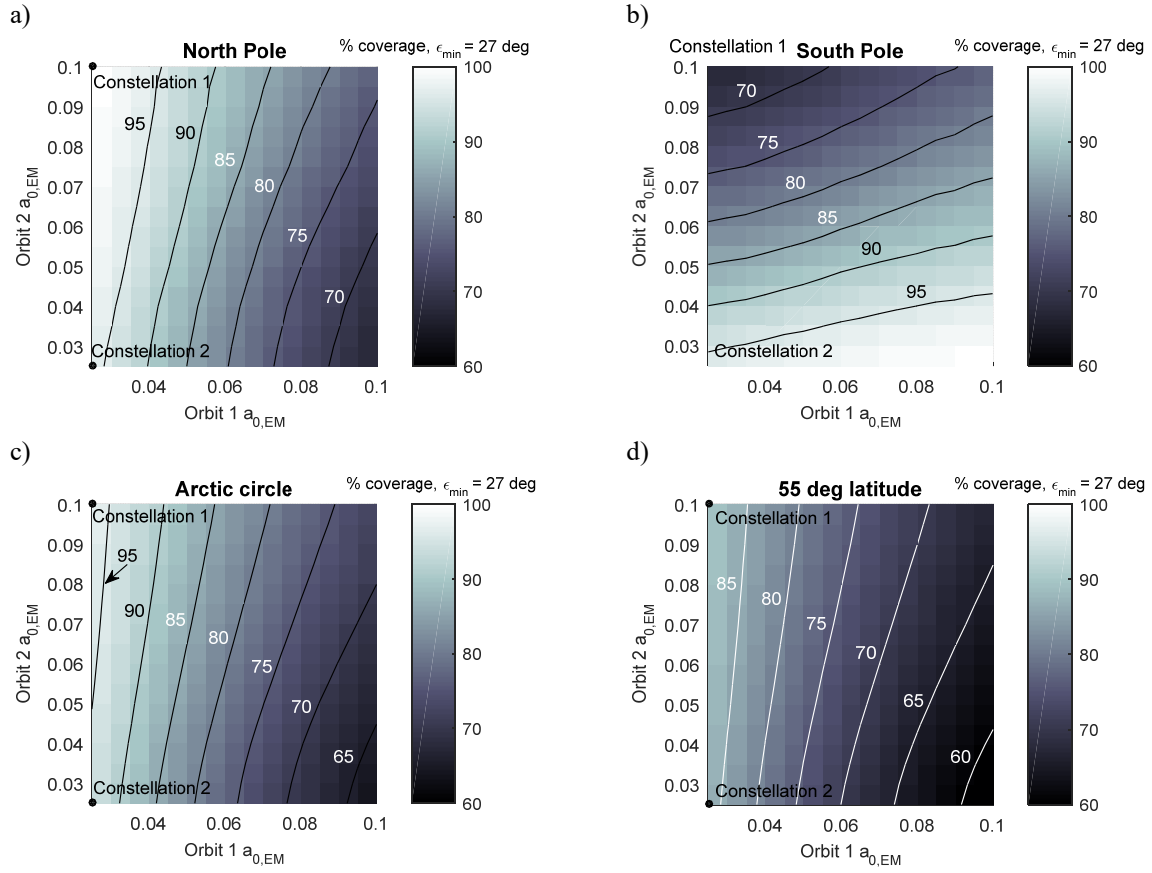


**Figure 6 Percentage temporal coverage from clover-shaped orbit constellation. a) North Pole. b) South Pole. c) Arctic circle. d) 55 deg latitude.**

**Table 1 Percentage temporal coverage from clover-shaped orbit constellation.**

Latitude	Constellation 1	Constellation 2
North Pole	99.6	96.3
South Pole	66.3	96.3
Arctic circle	96.4	93.7
55 deg	89.1	86.7

### **Constellation 1**

The first constellation with  $a_{0,EM} = 0.025$  for orbit 1 and  $a_{0,EM} = 0.1$  for orbit 2 that provides near-continuous coverage (99.6 percent, see Table 1) of the North Pole (or, when mirrored in the  $(x, y)$ -plane, of the South Pole) appears in Figure 7a, with its coverage of the North and South Poles in terms of elevation angle over time appearing in Figure 7c and d. From the top-plot in Figure 7d it is clear that, although continuous coverage at  $\epsilon_{lim} = 27$  deg of the North Pole is not achieved by this constellation, continuous coverage can be achieved when

lowering the minimum elevation angle to a value of 20 deg, which matches the spatial coverage requirements of the previously proposed Polar Communications and Weather (PCW) mission at the North Pole and 55 deg latitude [23]. The coverage over lower latitudes is also provided in Table 1 with more details appearing in Figure 8. Figure 8a illustrates the total useful observation time over the first orbital period. Where the lines flatten, neither of the two spacecraft is in view of the location or latitude under consideration. The actual observation time can then be translated into a percentage coverage, see Figure 8b. This percentage starts at 100 percent because at the initial time the spacecraft are assumed to be at their most out-of-plane position, see Figure 7a, and from this position all four locations considered in Figure 8 are in view of one of the two spacecraft. Over time, the percentage decreases and oscillates, but after one year converges to the value as depicted in Figure 7b, which uses a mesh of 1 deg in longitude and latitude. Finally, Figure 8c provides (for the North Pole only) information about the altitude and spatial resolution from the constellation. The spatial resolution is computed assuming a nadir-pointing payload and that the resolution is limited by diffraction only. Under those assumptions, the resolution is a function of the observable wavelength, imager aperture diameter and orbit altitude only and scales linearly with these parameters. Because the difference in orbit altitude between the four different locations/latitudes of Figure 8a and b is very small, the results for the North Pole (as in Figure 8c) are representative for the resolution and altitude for the other three locations/latitudes. Furthermore, the results in Figure 8c are obtained assuming observations in the visible part of the spectrum (0.5  $\mu\text{m}$ ) and for an imager aperture diameter of 0.5 m. However, the resolution for other observations can be easily deduced from Figure 8c due to the previously mentioned linear relation: for example, for observations in the infrared part of the spectrum, the resolution increases by a factor six and for a twice as large aperture diameter the resolution decreases by a factor of two. To get an idea of more realistic performances than the diffraction limited resolution presented in Figure 8c, the EPIC camera onboard the NOAA/NASA DSCOVR mission serves as a good example. At approximately 1.5 Mkm from the Earth, this imager enables a theoretical resolution of 8 km with an effective resolution of 10-15 km (depending on the channel) at a mass of 63.2 kg (including the computer)<sup>56</sup>. Again assuming a linear relation between the resolution and altitude, the EPIC camera shows that a maximum spatial resolution in the order of 3-5 km should be achievable from the clover-shaped orbit constellation. Other comparisons can be made with the SEVIRI imager on the Meteosat Second Generation (MSG) spacecraft, which

---

<sup>5</sup> WMO OSCAR | Details for Instrument EPIC (DSCOVR), <http://www.wmo-sat.info/oscar/instruments/view/793>, Accessed 24 June 2016

<sup>6</sup> DSCOVR: Deep Space Climate Observatory, <http://www.nesdis.noaa.gov/DSCOVR/>, Accessed 24 June 2016

provides down to 1 km resolution in the visible spectrum<sup>7</sup> from geostationary orbit (GEO), and the FCI camera on the Meteosat Third Generation (MTG) spacecraft, which provides down to 0.5 km resolution<sup>8</sup> from GEO. Both imagers show that resolutions of 5-10 km should be achievable from the clover-shaped orbits.

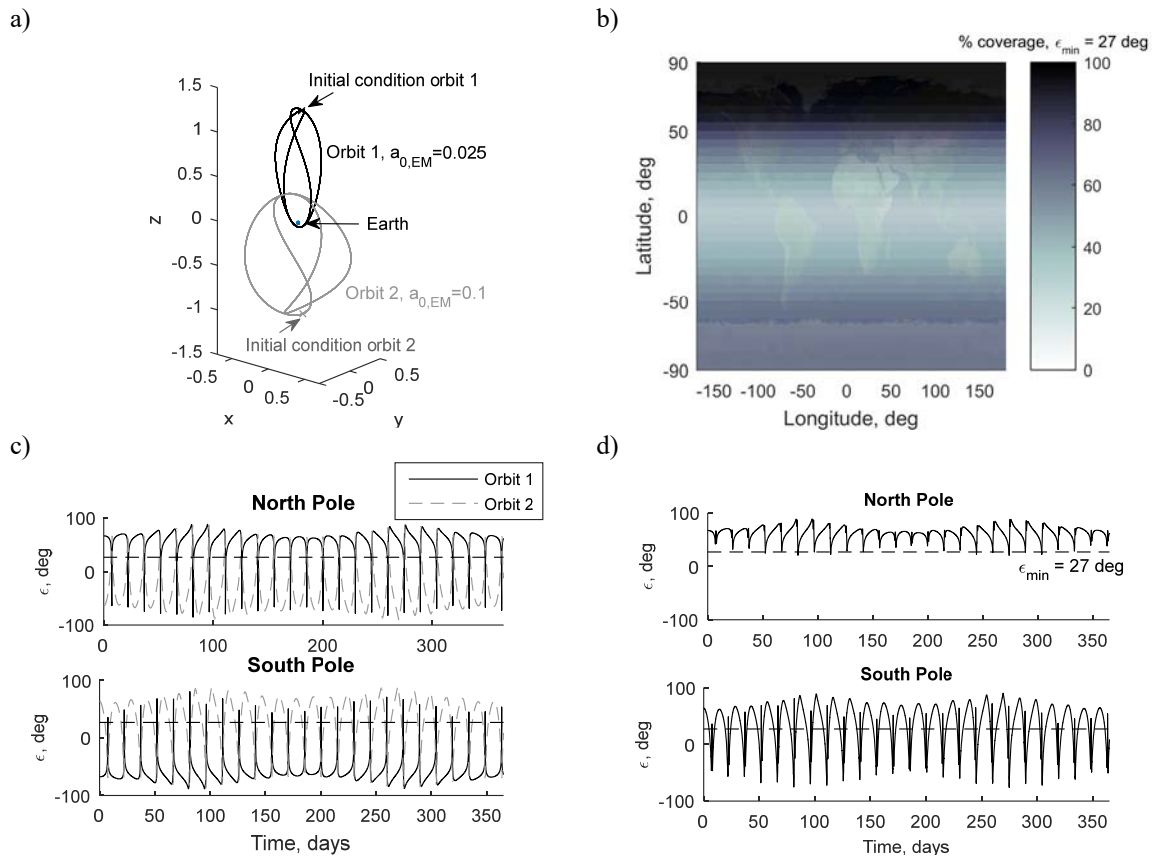


**Figure 7 Clover-shaped orbits, constellation 1. a) Constellation. b) Percentage temporal coverage. c) Elevation angle at North and South Poles. d) As subplot c) but best elevation angle over time.**

<sup>7</sup> WMO: OSCAR | Details for Instrument SEVIRI, <http://www.wmo-sat.info/oscar/instruments/view/503>, Accessed 16 August 2016

<sup>8</sup> WMO: OSCAR | Details for Instrument FCI, <http://www.wmo-sat.info/oscar/instruments/view/138>, Accessed 16 August 2016

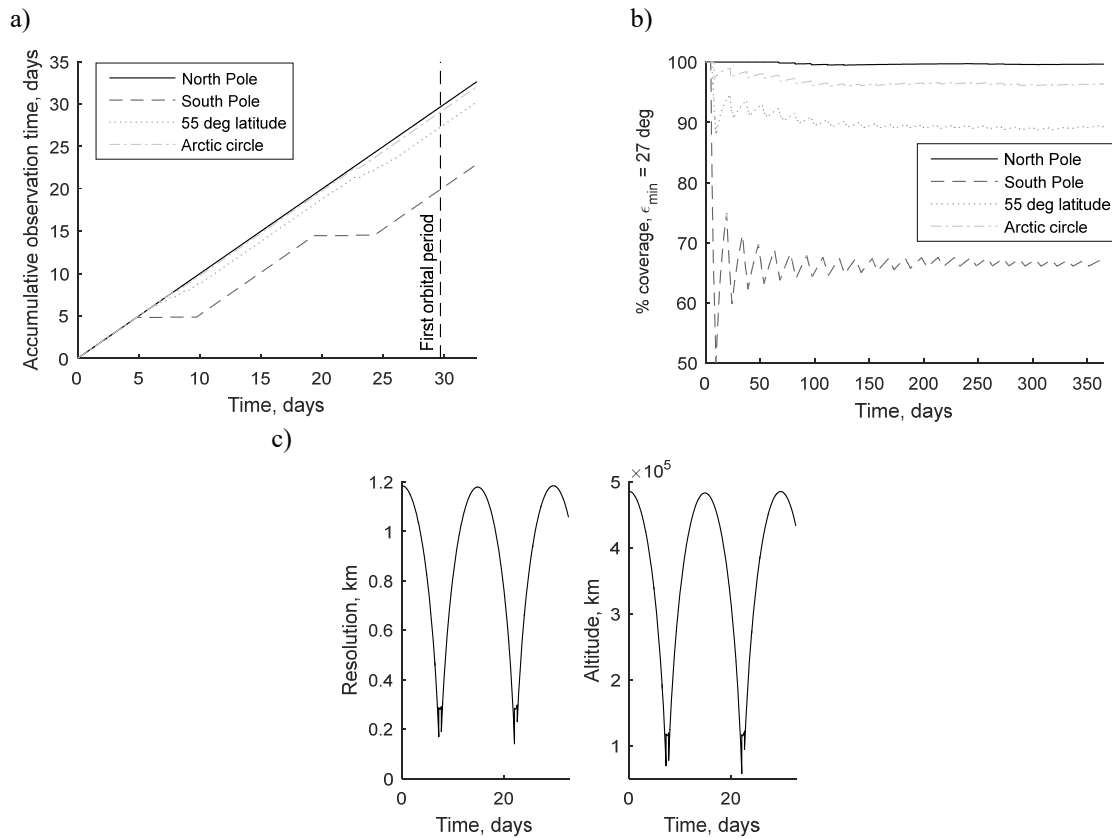


**Figure 8 Clover-shaped orbits, constellation 1. a) Accumulative observation time during first orbit. b) Percentage temporal coverage. c) Resolution and altitude (North Pole).**

### *Constellation 2*

Although constellation 1 achieves very good coverage of one of the Poles, coverage of the other Pole is poor (only 66.3 percent, see Table 1). Therefore constellation 2 is proposed as an alternative, see Figure 9, which consists of a mirrored constellation of two clover-shaped orbits, both with  $a_{0,EM} = 0.025$ . Again, assuming  $\epsilon_{\lim} = 27$  deg this constellation achieves a coverage of 96.3 percent for *both* Poles (97.4 percent for  $\epsilon_{\lim} = 20$  deg) with >90 percent temporal coverage of the entire Arctic and Antarctic regions. Details, similar to the ones presented in Figure 7 and Figure 8 for constellation 1 are provided in Figure 9 and Figure 10 for constellation 2. These figures show a significant improvement in the coverage of the South Pole at similar resolution values as for constellation 1.

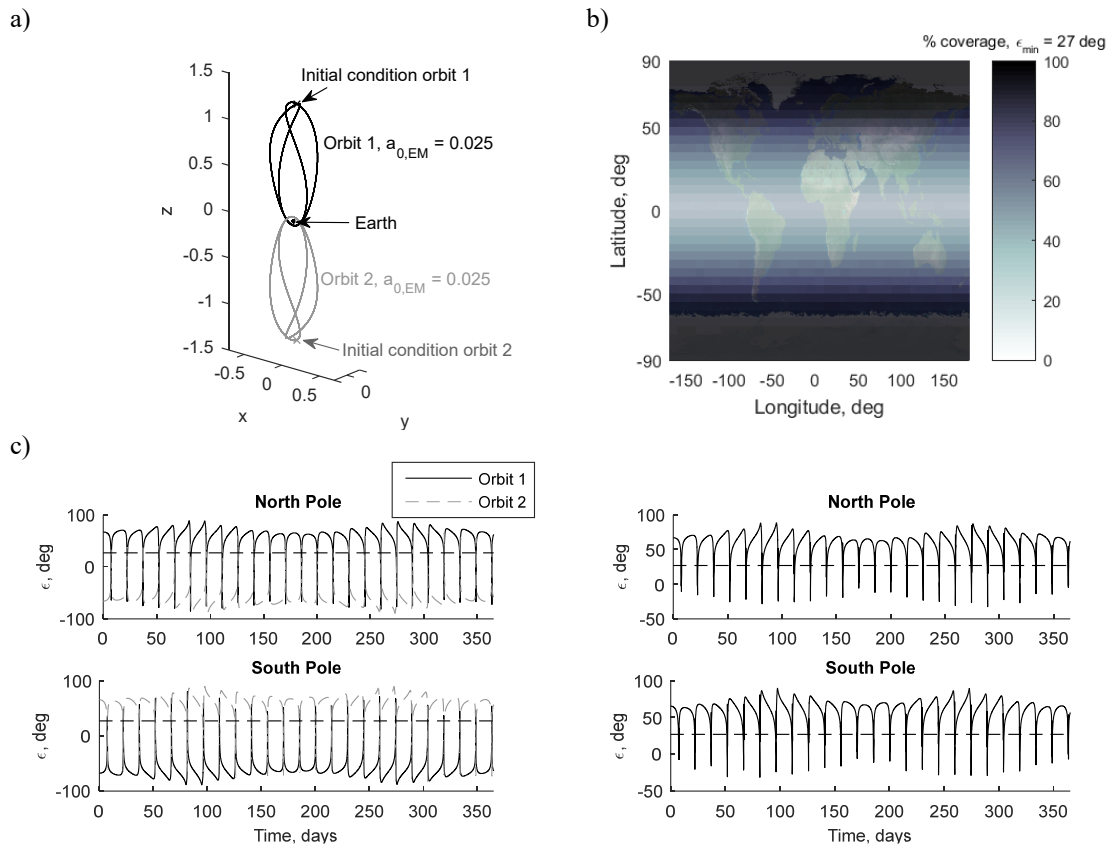


**Figure 9 Clover-shaped orbits, constellation 2. a) Constellation. b) Percentage temporal coverage. c) Elevation angle at North and South Poles. d) As subplot c) but best elevation angle over time.**

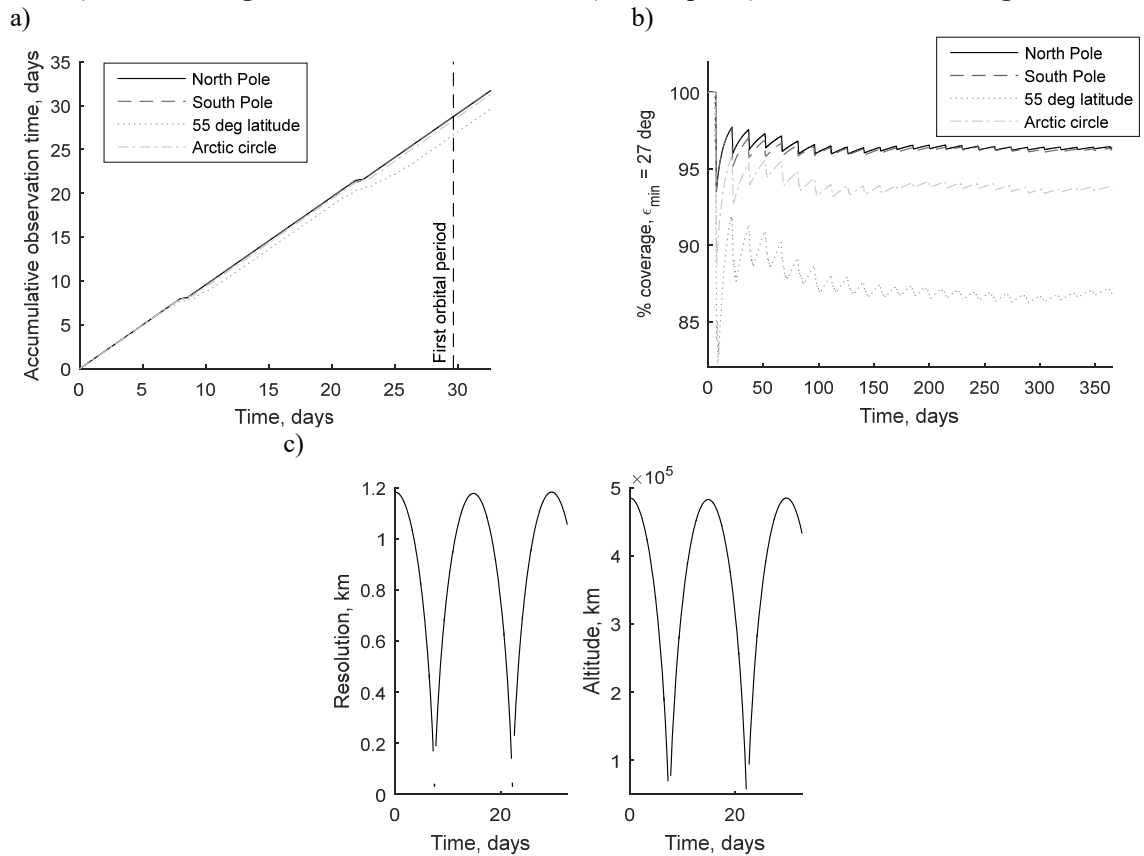


**Figure 10 Clover-shaped orbits, constellation 2. a) Accumulative observation time during first orbit. b) Percentage temporal coverage. c) Resolution and altitude (North Pole).**

## B. Vertical Lyapunov orbits for lunar observation

The far-side of the Moon has long held the interest of scientists and is considered as one of the possible locations for a future (permanent) human base. One of the most striking features on the far side of the Moon is the South Pole Aitken Basin (coordinates of its center are  $53^{\circ}\text{S } 169^{\circ}\text{W}$ ), a huge impact crater which is believed to hold clues to the history of the Moon and allows access to the deeper layers of the lunar crust.<sup>9</sup> Regarding the human base, the lunar South Pole (in particular the rim of the Shackleton crater,  $89.9^{\circ}\text{S } 180^{\circ}\text{W}$ ) is often mentioned as a potential location as it is an area of near-permanent sunlight, providing access to power, and water ice may be present in the continuously shaded areas of the crater interior [24]. For support of the occupants of the base, a continuous communication link with Earth will be essential, which is not guaranteed from the South Pole. Traditionally, natural halo orbits at the  $L_2$  point are proposed to this end [25, 26], but a single spacecraft cannot provide sufficient coverage. Studies have therefore been conducted to use a combination of halo, vertical and butterfly families at the Earth-Moon  $L_1$  and  $L_2$  points, showing that several combinations of two of these orbits can achieve continuous coverage of the South Pole [27]. Other studies have investigated the use of a solar sail to maintain a non-Keplerian orbit below the South Pole to achieve continuous coverage and line-of-sight with the Earth with a single spacecraft [28-31]. While all these studies focus on coverage of the South Pole only, the solar sail vertical Lyapunov orbits of Figure 5 will be investigated for continuous coverage of both the lunar South Pole *and* the center of the South Pole Aitken Basin (hereafter referred to as Aitken Basin for brevity). Furthermore, compared to the solar sail trajectories below the South Pole presented in References [28-31], which use an optimal steering law, the orbits in Figure 5 greatly simplify the steering of the sail through the assumed fixed solar sail attitude with respect to the Sun. Future investigations may provide a further trade-off between these different concepts in terms of altitude, elevation angles, and so on.

To determine which constellation of vertical Lyapunov orbits would perform best for continuous coverage of the lunar South Pole and the center of the Aitken Basin, a grid search is performed over a combination of characteristic accelerations for each of the orbits, where the spacecraft are phased half a period apart, such that one spacecraft starts at the tip of the orbit above the Earth-Moon plane at time  $t = 0$ , whereas the other

---

<sup>9</sup> Lunar and Planetary Institute, [Feasibility Assessment of All Science Concepts within South Pole-Aitken Basin](#), Accessed 31 July 2016

spacecraft starts at the other tip of the orbit, below the Earth-Moon plane. Figure 11a and b shows the best performing constellation, which consists of two orbits both with  $a_{0,EM} = 0.1$  and  $\gamma = -35.26$ . In this case, a minimum elevation of  $\varepsilon_{lim} = 15$  deg is assumed in compliance with References [27, 30, 31]. The elevation profiles in Figure 11c and d then show that the constellation in subplot a) can achieve continuous coverage of both the South Pole and the Aitken Basin. Coverage of the rest of the Moon is reasonable, see Figure 11e, except for a spot around the lunar equator on the Earth-facing side of the Moon. Finally, information about the spatial resolution from and altitude of the constellation is shown in Figure 11f. Note that Figure 11f shows the results for the South Pole only, but that near-identical results can be obtained for the center of the Aitken Basin due to the relatively high altitude of the orbits. Finally, note that plots such as those provided for the Earth-centered orbits in Figure 8a, b and Figure 10a, b are omitted because continuous, i.e., 100 percent temporal coverage is achieved, which would just result in straight lines in similar plots.

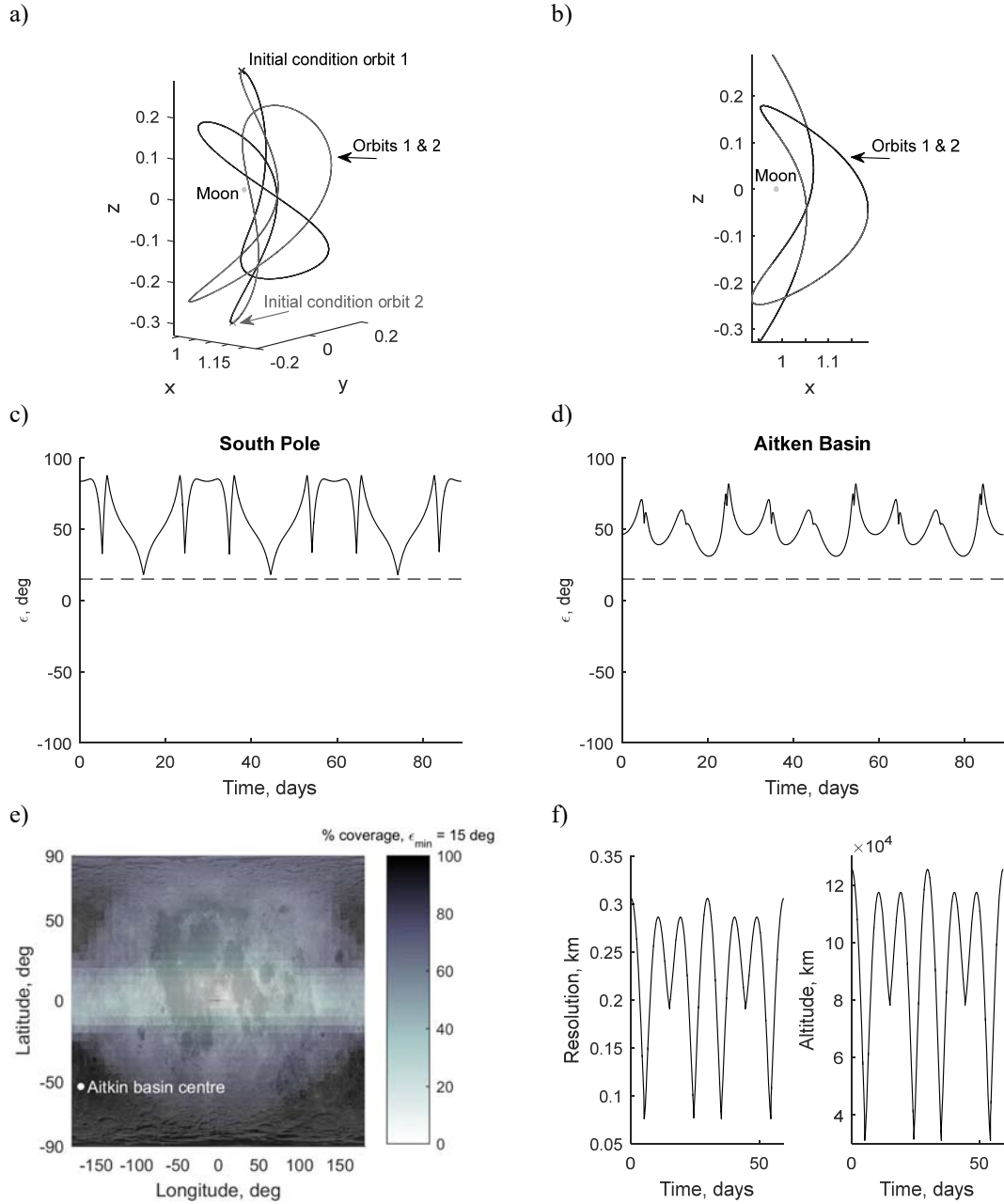


**Figure 11 Constellation of solar sail L<sub>2</sub> vertical Lyapunov orbits. a,b) Constellation. c,d) Best elevation angle at South Pole (c) and center of Aitken Basin (d). e) Percentage temporal coverage. f) Resolution and altitude (South Pole).**

## V. High-fidelity model

The constellations of orbits in the previous section were designed within the framework of the circular restricted three-body problem, neglecting the gravitational attraction of the Sun, the offset between the ecliptic and the Earth-Moon planes as well as the orbital eccentricities of the Earth and the Moon. As such, further analyses are required to demonstrate that the orbits still hold under these higher-fidelity conditions. Therefore, in this section, the orbits of Section IV will be investigated while taking into account these periodic perturbations

where the period of some perturbations coincide with the synodic lunar month (the solar gravity), while other perturbations act on a time-scale different from the synodic lunar month (plane offset and Earth and lunar eccentricities). These two types of perturbations will therefore also affect the orbits differently, where the solar gravity will just displace the orbit, while the other perturbations will cause the periodicity of the solar sail orbits to disappear.

In Sections V.A though V.D the model used for each perturbation will be presented, followed by a summary of the new higher-fidelity dynamics in Section V.E. The technique used to find trajectories that remain close to the nominal periodic orbits under the higher-fidelity dynamics, a multiple shooting differential correction algorithm, will be discussed in Section V.F with the results in terms of the effect of each perturbation separately as well as the effect of all perturbations combined will be presented in Section V.G.

### A. Solar gravity

Using the vector definitions illustrated in Figure 12a, the perturbing acceleration due to the Sun's gravity is given by:

$$\mathbf{a}_4 = \frac{\partial \Omega_4}{\partial \mathbf{r}}, \quad \Omega_4 = \mu_4 \left( \frac{1}{|\mathbf{r}_{s,4}|} - \frac{\mathbf{r} \cdot \mathbf{r}_4}{|\mathbf{r}_4|^3} \right) \quad (6)$$

with  $\mu_4 = m_s / (m_E + m_M) = 3.2893 \times 10^5$  (where  $m_s$ ,  $m_E$  and  $m_M$  are the masses of the Sun, Earth and Moon, respectively). Furthermore,  $\mathbf{r}_4 = -\mathbf{r}_4 \cdot \hat{\mathbf{S}}$  is the position vector of the Sun and  $\mathbf{r}_{s,4} = \mathbf{r}_4 - \mathbf{r}$  is the position vector from the sail to the Sun.

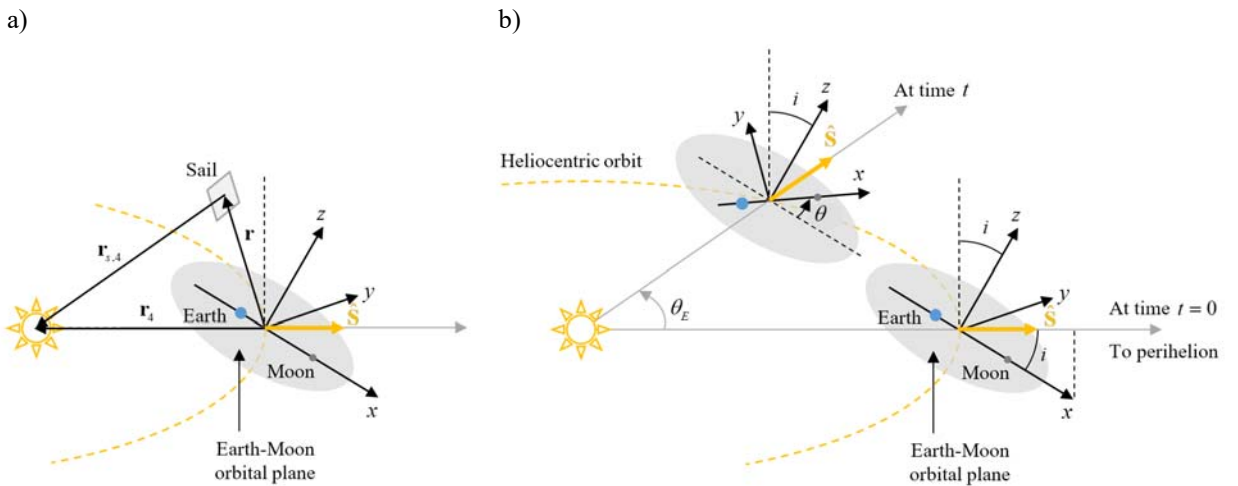


**Figure 12 Schematic to support the definitions of the solar gravity perturbation and the offset between the ecliptic and Earth-Moon planes.**

## B. Plane offset

The offset between the ecliptic and the Earth-Moon planes of  $i = 5.145$  deg can be modelled through a new definition for the Sun-vector,  $\hat{\mathbf{S}}$ , see Figure 12b:

$$\hat{\mathbf{S}} = [S_x \quad S_y \quad S_z]^T = R_z(-\theta) R_y(-i) R_z(\theta_E - \theta_{E,0}) \begin{bmatrix} 1 \\ 0 \\ 0 \end{bmatrix} = R_{tot} \begin{bmatrix} 1 \\ 0 \\ 0 \end{bmatrix}. \quad (7)$$

Equation (7) assumes that at the start of the orbital analyses, at time  $t = 0$ , the Earth-Moon system is at a certain true anomaly,  $\theta_E = \theta_{E,0}$ , in its heliocentric orbit and that the sunlight-vector  $\hat{\mathbf{S}}$  points along the  $x$ -axis of the synodic reference frame. Then, three rotations are applied: the first rotation,  $R_z(\theta_E - \theta_{E,0})$ , around the  $z$ -axis over an angle  $\theta_E - \theta_{E,0}$ , accounts for the orbital motion of the Earth-Moon system around the Sun; the second rotation,  $R_y(-i)$  accounts for the offset between the ecliptic and Earth-Moon planes; and the final rotation,  $R_z(-\theta)$  accounts for the rotation of the  $\hat{\mathbf{S}}$ -vector due to the orbital motion of the Earth and Moon around each other with  $\theta$  the true anomaly of the Moon in its orbit around the Earth. Note that the combination of the rotation matrices  $R_z(-\theta)$  and  $R_z(\theta_E - \theta_{E,0})$  replaces the single rotation matrix  $R_z(\Omega_S t)$  in Eq. (2). When, for now, assuming zero eccentricities for the Earth and Moon, the Moon's true anomaly equals the dimensionless time and the true anomaly of the Earth can be computed by transforming this dimensionless time in the CR3BP to dimensional time and subsequently solving Kepler's equation using Newton's method [16].

The new Sun-vector of Eq. (7) feeds into the solar sail induced acceleration vector in Eq. (3) as well as into the fourth body perturbation acceleration in Eq. (6) through the vector  $\mathbf{r}_4$ . Note that, for the solar sail induced acceleration, the attitude *with respect to the Sun-direction*,  $\hat{\mathbf{n}}_S$ , is kept constant such that the normal vector with respect to the synodic frame in Eq. (3) is given by:

$$\hat{\mathbf{n}} = R_{tot} \hat{\mathbf{n}}_S. \quad (8)$$

When again assuming zero eccentricities of the Earth and the Moon, the Cartesian components of the unit vector  $\hat{\mathbf{S}}$  during the year are provided in Figure 13. The figure shows a rapid change in the  $x$ - and  $y$ -components of the  $\hat{\mathbf{S}}$ -vector due to the rotation of the Earth-Moon system and a much slower oscillation in the  $z$ -component due to the offset between the Earth-Moon and ecliptic planes.

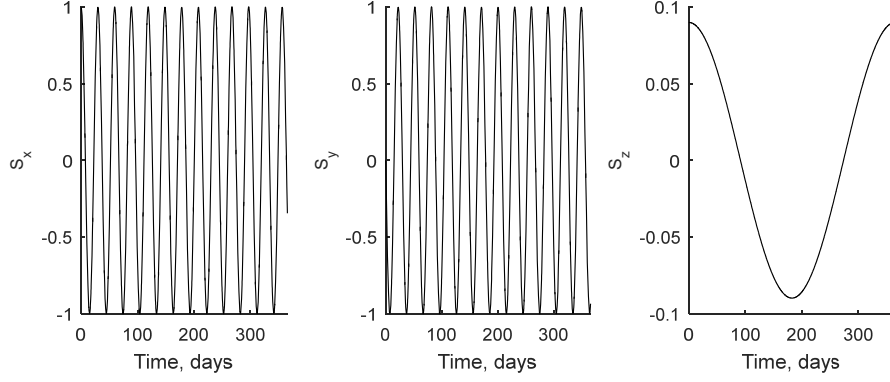


**Figure 13 Time-varying Cartesian components of the Sun-vector  $\hat{\mathbf{S}}$  in the synodic reference frame for a 5.145 deg offset between the Earth-Moon and ecliptic planes.**

### C. Earth's eccentricity

The eccentricity of the Earth,  $e_E = 0.0167$ , introduces a change to the Sun's position vector,  $\mathbf{r}_4 = -r_4 \cdot \hat{\mathbf{S}}$ , see Figure 12 with  $\hat{\mathbf{S}}$  from Eq. (7), as the magnitude of this vector is no longer constant at 1 au, but varies according to

$$r_4 = \frac{a_E (1 - e_E^2)}{1 + e_E \cos \theta_E} \quad (9)$$

with  $a_E = 1$  au the Earth's semi-major axis and  $\theta_E$  the Earth's true anomaly. In these analyses it is assumed that the Earth is at its perihelion at the initial time, i.e.,  $\theta_{E,0} = 0$  in Eq. (7). Note again that, to find the Earth's true anomaly, Kepler's equation needs to be solved at each integration step. The varying Sun-Earth distance not only affects the solar gravity perturbation potential in Eq. (6), but also the magnitude of the solar sail acceleration, which needs to be rescaled as:

$$\mathbf{a}_s = a_{0,EM} \left( \frac{\text{au}}{r_4} \right)^2 (\hat{\mathbf{S}} \cdot \hat{\mathbf{n}})^2 \hat{\mathbf{n}}. \quad (10)$$

### D. Lunar eccentricity

The final perturbation to account for is the eccentricity of the Moon,  $e = 0.0549$ . For this, the dynamical framework of the circular restricted three-body problem in Section II is replaced by the framework of the solar sail elliptic restricted three-body problem (ER3BP) [32]:

$$\begin{aligned}
X'' - 2Y' &= \frac{1}{1 + e \cos \theta} \left( \frac{\partial \Omega_E}{\partial X} + a_{s,X} \right) \\
Y'' + 2X' &= \frac{1}{1 + e \cos \theta} \left( \frac{\partial \Omega_E}{\partial Y} + a_{s,Y} \right) . \\
Z'' + Z &= \frac{1}{1 + e \cos \theta} \left( \frac{\partial \Omega_E}{\partial Z} + a_{s,Z} \right)
\end{aligned} \tag{11}$$

The prime in Eq. (11) indicates the derivative with respect to the Moon's true anomaly,  $\theta$ , and the solar sail state vector,  $\mathbf{X} = [X \ Y \ Z \ X' \ Y' \ Z']^T$ , is defined in a *pulsating* synodic reference frame (such that the Earth and the Moon are always located at  $\mathbf{X} = [1 - \mu \ 0 \ 0]^T$  and  $\mathbf{X} = [-\mu \ 0 \ 0]^T$ , respectively). The transformation required to go back to the synodic reference frame coordinates,  $\mathbf{x}(x, y, z)$  is:  $\mathbf{x} = \frac{1 - e^2}{1 + e \cos \theta} \mathbf{X}$ .

Furthermore, in Eq. (11),

$$\Omega_E = \frac{1}{2} (X^2 + Y^2 + Z^2) + \frac{1 - \mu}{|\mathbf{r}_1|} + \frac{\mu}{|\mathbf{r}_2|} \tag{12}$$

and  $a_{s,X}$ ,  $a_{s,Y}$  and  $a_{s,Z}$  are the solar sail acceleration components in  $X$ -,  $Y$ - and  $Z$ -direction, respectively.

Due to the eccentricity of the Moon and the switch to the true anomaly of the Moon as the independent variable, the time (required to compute the Earth's true anomaly in Eq. (7)) needs to be computed from [33]:

$$E = \tan^{-1} \left( \frac{\sqrt{1 - e^2} \sin \theta}{e + \cos \theta} \right) \tag{13}$$

$$M = E - e \sin E \tag{14}$$

$$t = \text{mod}(M, 2\pi) + 2\pi \times \text{floor} \left( \frac{\theta}{2\pi} \right), \tag{15}$$

where  $E$ ,  $M$  and  $t$  are the Moon's eccentric anomaly, mean anomaly and dimensionless time, respectively. Transforming the result from Eq. (15) to dimensional time, Kepler's equation can once again be solved to find the Earth's true anomaly.

## E. High-fidelity dynamics

The previous sections have discussed the models used for each of the perturbations separately. To obtain a proper overview of how each perturbation feeds into the dynamics, the below gives a summary of the new high-fidelity dynamical model, starting with the equations of motion:

$$\begin{aligned}
X'' - 2Y' &= \frac{1}{1 + e \cos \theta} \left( \frac{\partial \Omega_E}{\partial X} + a_{s,x} + \frac{\partial \Omega_4}{\partial X} \right) \\
Y'' + 2X' &= \frac{1}{1 + e \cos \theta} \left( \frac{\partial \Omega_E}{\partial Y} + a_{s,y} + \frac{\partial \Omega_4}{\partial Y} \right) . \\
Z'' + Z &= \frac{1}{1 + e \cos \theta} \left( \frac{\partial \Omega_E}{\partial Z} + a_{s,z} + \frac{\partial \Omega_4}{\partial Z} \right)
\end{aligned} \tag{16}$$

where

$$\Omega_E = \frac{1}{2} (X^2 + Y^2 + Z^2) + \frac{1 - \mu}{|\mathbf{r}_1|} + \frac{\mu}{|\mathbf{r}_2|} , \tag{17}$$

$$\mathbf{a}_s = a_{0,EM} \left( \frac{\text{au}}{r_4} \right)^2 (\hat{\mathbf{S}} \cdot \hat{\mathbf{n}})^2 \hat{\mathbf{n}} , \tag{18}$$

$$\Omega_4 = \mu_4 \left( \frac{1}{|\mathbf{r}_{s,4}|} - \frac{\mathbf{r} \cdot \mathbf{r}_4}{|\mathbf{r}_4|^3} \right) \tag{19}$$

with  $\mathbf{r} = [X \ Y \ Z]^T$ ,  $\mathbf{r}_1 = [X + \mu \ Y \ Z]^T$ ,  $\mathbf{r}_2 = [X - (1 - \mu) \ Y \ Z]^T$ ,  $\mathbf{r}_{s,4} = \mathbf{r}_4 - \mathbf{r}$ , and  $a_{0,EM}$  defined at 1 au. Furthermore, the Sun's position vector is given by

$$\mathbf{r}_4 = -r_4 \hat{\mathbf{S}} = -\frac{a_E (1 - e_E^2)}{1 + e_E \cos \theta_E} \hat{\mathbf{S}} \tag{20}$$

with

$$\hat{\mathbf{S}} = R_z(-\theta) R_y(-i) R_z(\theta_E - \theta_{E,0}) \begin{bmatrix} 1 \\ 0 \\ 0 \end{bmatrix} = R_{tot} \begin{bmatrix} 1 \\ 0 \\ 0 \end{bmatrix} . \tag{21}$$

Finally, the sail's normal vector is equal to:

$$\hat{\mathbf{n}} = R_{tot} \hat{\mathbf{n}}_s = R_{tot} \begin{cases} [1 \ 0 \ 0]^T & \text{Clover-shaped orbits} \\ R_y(-\gamma) [1 \ 0 \ 0]^T & \text{Vertical Lyapunov orbits} \end{cases} \tag{22}$$

In order to compute the true anomaly of the Earth,  $\theta_E$ , at each integration step, i.e., for the current value of the Moon's true anomaly,  $\theta$ , Kepler's equation is solved numerically. For this, the current dimensional time is required, which is computed through:

$$E = \tan^{-1} \left( \frac{\sqrt{1 - e^2} \sin \theta}{e + \cos \theta} \right) \tag{23}$$

$$M = E - e \sin E \tag{24}$$

$$t = \text{mod}(M, 2\pi) + 2\pi \times \text{floor} \left( \frac{\theta}{2\pi} \right) \tag{25}$$

where the dimensionless time  $t$  in Eq. (25) needs to be converted to dimensional time for use in solving Kepler's equation.

#### F. Multiple shooting differential correction scheme

In order to find solar sail orbits in close proximity to the periodic orbits of Section V.A but within the dynamical framework of Eq. (16), a multiple shooting differential correction (MSDC) scheme is implemented, similar to the works in References [34-36]. MSDC divides an initial guess of the trajectory into segments by defining patch points at appropriate locations. Here, the orbits in the circular restricted three-body problem are used as initial guess and a continuation scheme is applied to slowly introduce the higher fidelity model. The advantage of starting from an orbit (with associated time vector) that exists for zero lunar eccentricity,  $e = 0$ , is that the Moon's true anomaly is equal to the dimensionless time. This eliminates the transformation of the velocity and acceleration states from time units to angle units. Once the initial guess has been divided into segments, two differential correction 'levels' are applied [34]: the first level adjusts the velocities at each patch point along the trajectory using a single-shooting differential corrector. The result is a continuous trajectory that must perform a  $\Delta V$  at each patch point in order to follow the trajectory. The second level then adjusts the positions and epochs at each patch point using a least-squares method in a way that the total  $\Delta V$  along the trajectory is minimized. The result of the MSDC scheme is a trajectory that holds under the dynamics of Eq. (16). In this investigation, accuracies on the mismatch in position at each patch point of  $10^{-7}$  (dimensionless units, which corresponds to 38 m) is used and an accuracy on the mismatch in velocity *summed* over all patch points of  $5 \times 10^{-5}$  (dimensionless units, which corresponds to 0.05 m/s) is used.

#### G. Results

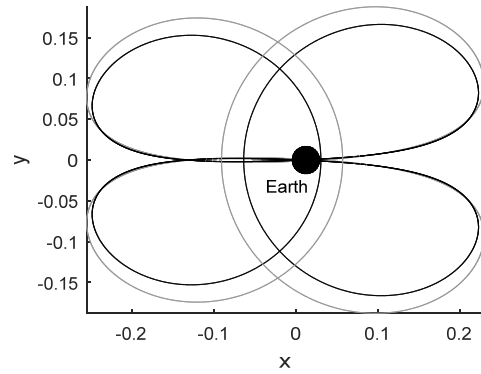
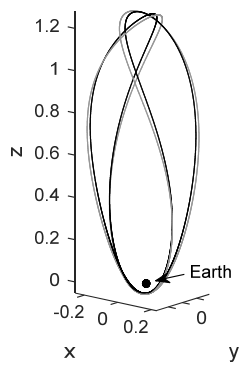
The results of the high-fidelity analyses for the orbits used in the clover-shaped constellations in Section IV.A appear in Figure 14 and Figure 15 where the subplots increase the fidelity of the dynamics one perturbation at a time. Note that Figure 14 and Figure 15 show the effect on the clover-shaped orbits with  $a_{0,EM} = 0.025$  (see the black orbit in Figure 7a) and  $a_{0,EM} = 0.1$  (the gray orbit in Figure 7a, but mirrored in the  $(x, y)$  -plane). In subplots a), only the solar gravity is considered and is added to the dynamics through a continuation on the value for  $\mu_4$ , starting from the unperturbed orbits (shown by black lines throughout Figure 14 and Figure 15). Note that, for now, the plane offset is not taken into account, which means that periodicity of the orbits is maintained. The effect of the solar gravity on the orbit is relatively small, which is quantified

through the difference in Earth-sail vector magnitude in the top left plots in Figure 16a and b where  $r_1$  and  $r_{1,0}$  are the Earth-sail distances for the perturbed and unperturbed orbits, respectively.

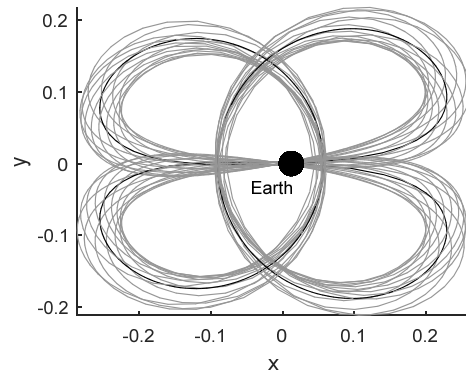
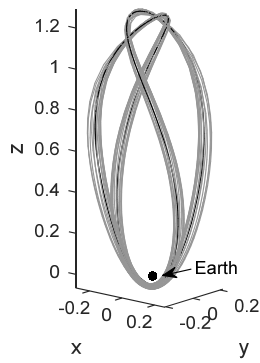
The next perturbation added is the offset between the Earth-Moon and ecliptic planes. The combined effect of the solar gravity and plane offset is shown in subplot b) of Figure 14 and Figure 15 with the difference in Earth-sail distances in the top right plots of Figure 16a and b. These are the results of the MSDC scheme of Section V.F conducted over a timeframe of one year (i.e., approximately 14 revolutions in the clover-shaped orbits) and by employing a continuation on the value for  $\mu_4$  and  $i$ , simultaneously, again starting from the unperturbed orbits. When also adding the Earth's eccentricity to the dynamics (through a simultaneous continuation on  $\mu_4$ ,  $i$  and  $e_E$ ), the results in subplot c) of Figure 14 and Figure 15 and the bottom left plots in Figure 16a and b are obtained. While the inclination between the Earth-Moon and ecliptic planes significantly perturbs the orbit, the Earth's eccentricity does not perturb the orbits much further. Finally, the eccentricity of the Moon is added to the dynamics and results are created through a simultaneous continuation on  $\mu_4$ ,  $i$ ,  $e_E$  and  $e$  with the result in subplots d) of Figure 14 and Figure 15 and the bottom right plots in Figure 16a and b. Note that the orbital plots in Figure 14d and Figure 15d are provided in the synodic reference frame where the Earth moves along the  $x$ -axis, but that this movement is not significant enough for the Earth to be visible in Figure 14d and Figure 15d. While the combined effect of all perturbations is significant, the orbital shape of the clover-shaped orbits does not break down under their influence. Finally, although the trajectories appearing in Figure 14d and Figure 15d seem to suggest that the orbits intersect the Earth and the Moon, this is not the case. The minimum altitude of these orbits over time occurs for the clover-shaped orbit with  $a_{0,EM} = 0.025$  and is 4,169 km.

To assess the effect of the high-fidelity model on the performance of these orbits for high-latitude coverage of the Earth, similar analyses as in Section IV.A are conducted for the perturbed orbits presented in Figure 14d and Figure 15d (and their mirrored counterparts). The overall results are provided in Table 2. Table 2 provides the temporal coverage of both the orbits in the low-fidelity model (i.e., the CR3BP, see also Table 1) and the high-fidelity model for the four latitudes previously considered in Section IV.A. Comparing the percentages shows that the perturbations have only limited effect on the coverage: while in some instances the high-fidelity model allows a gain in temporal coverage (up to +0.1 percent), in general it causes a loss in coverage of up to -1.7 percent.

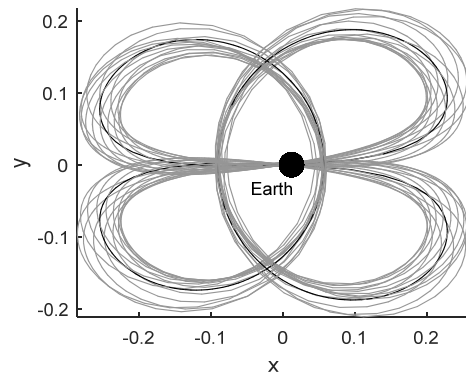
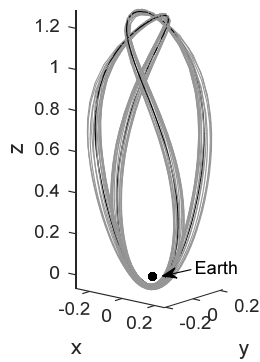
a)



b)



c)



d)

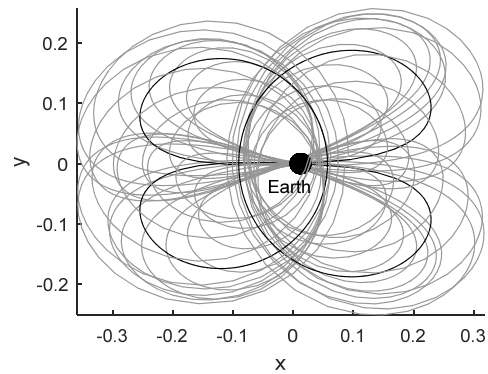
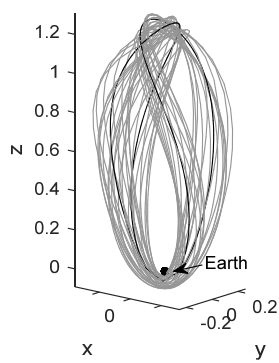
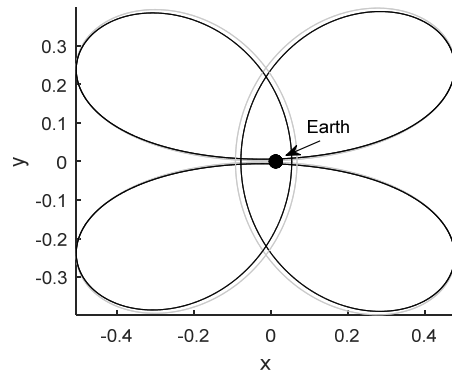
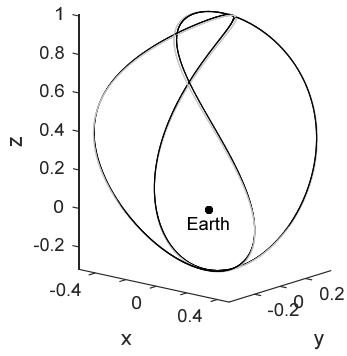
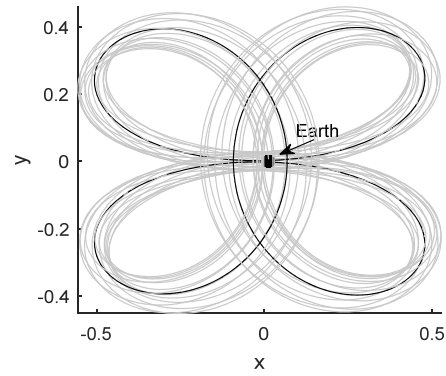
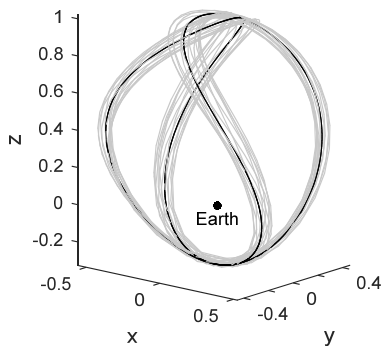


**Figure 14 Perturbed (gray) and unperturbed (black) clover-shaped orbit with  $a_{0,EM} = 0.025$  in synodic frame. a) Solar gravity. b) Solar gravity + plane offset. c) Solar gravity + plane offset + eccentricity Earth. d) All perturbations.**

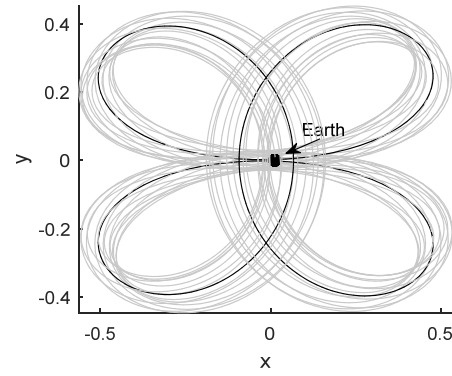
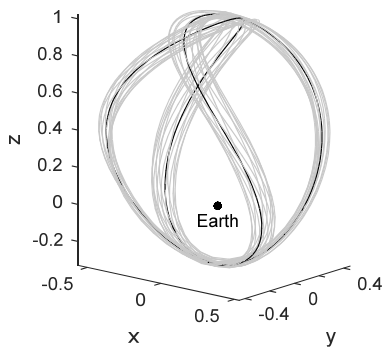
a)



b)



c)



d)

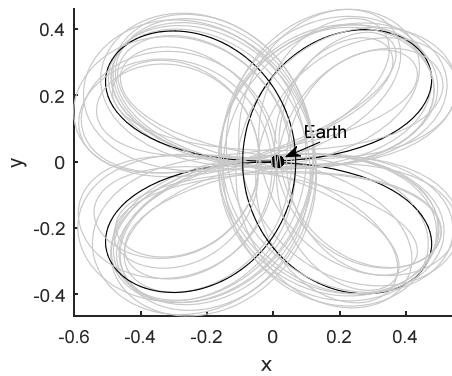
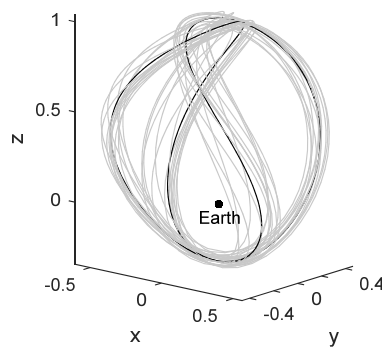
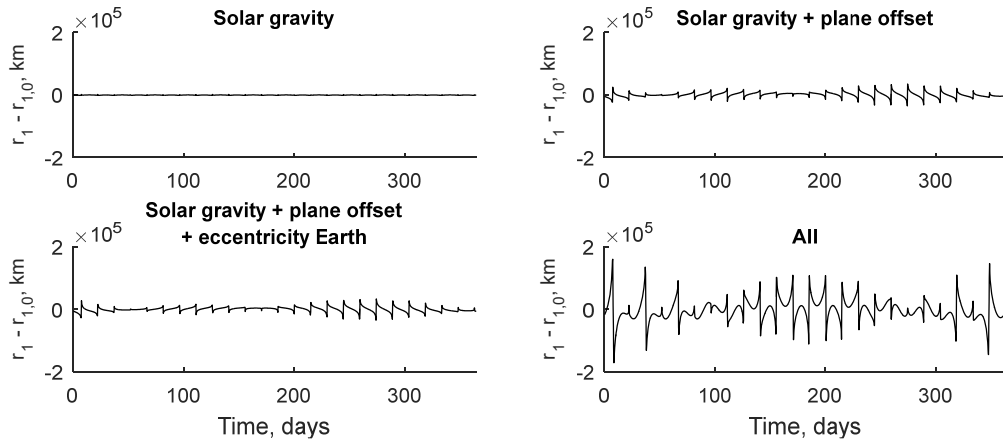
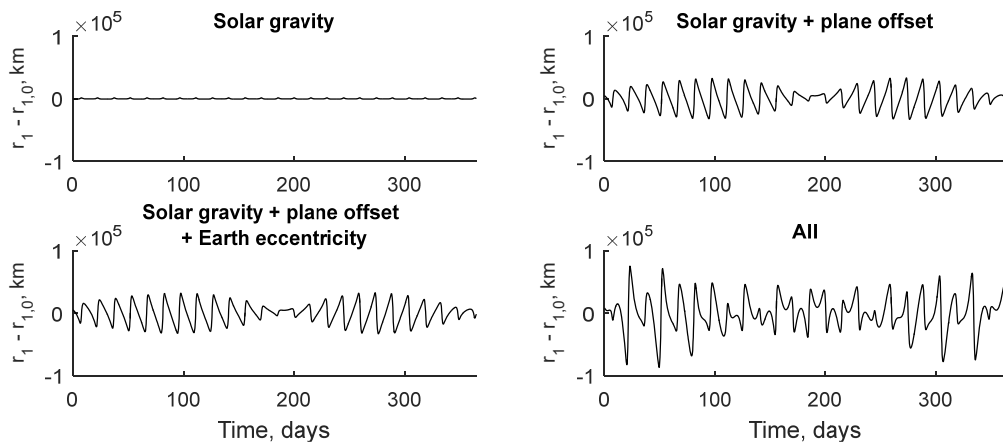


**Figure 15 Perturbed (gray) and unperturbed (black) clover-shaped orbit with  $a_{0,EM} = 0.1$  in synodic frame. a) Solar gravity. b) Solar gravity + plane offset. c) Solar gravity + plane offset + eccentricity Earth. d) All perturbations.**

a)



b)



c)

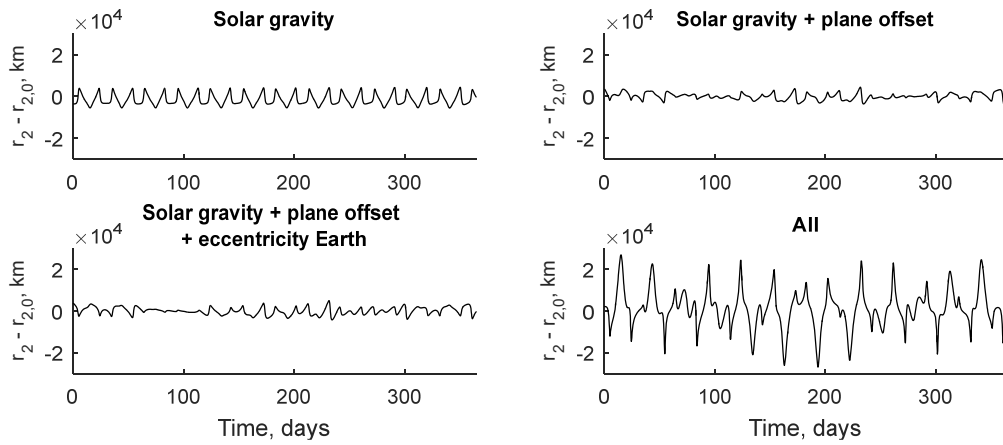


**Figure 16** Difference in Earth-sail or Moon-sail distance between perturbed and unperturbed orbits. **a,b)** Clover-shaped orbit with  $a_{0,EM} = 0.025$  (a) and  $a_{0,EM} = 0.1$  (b). **c)** Vertical Lyapunov orbit with  $a_{0,EM} = 0.1$ .

**Table 2 Percentage temporal coverage from clover-shaped orbits in low- and high-fidelity models.**

Latitude	Constellation 1		Constellation 2	
	CR3BP	High-fidelity	CR3BP	High-fidelity
North Pole	99.6	98.6 (-1.0)	96.3	95.5 (-0.8)
South Pole	66.3	64.6 (-1.7)	96.3	95.6 (-0.7)
Arctic circle	96.4	96.1 (-0.3)	93.7	92.7 (-1.0)
55 deg	89.1	89.2 (+0.1)	86.7	86.3 (-0.4)

Conducting similar analyses for the vertical Lyapunov orbits of the constellation in Section IV.B provides the results in Figure 17 and Figure 16c, again adding one perturbation at a time to the dynamics. Note that Figure 16c now shows the difference in Moon-sail distance where  $r_2$  and  $r_{2,0}$  are the Moon-sail distances for the perturbed and unperturbed orbits, respectively. Compared to the effect of the perturbations on the clover-shaped orbits, the solar gravity appears to have a bigger effect on the vertical Lyapunov orbits which seems partially corrected by the offset between the Earth-Moon and ecliptic planes. The Earth's eccentricity once again has only a minor effect, while the lunar eccentricity has a much greater effect due to the close proximity of the vertical Lyapunov orbits to the Moon. However, the constellation always remains above an altitude of 13,378 km.

Finally, the effect of the perturbations on the high-latitude coverage of the South Pole and center of the Aitken Basin is evaluated, which yields the results in Figure 18. While the Aitken Basin remains continuously visible, the minimum elevation above the South Pole drops below the minimum required elevation of 15 deg, but only for a total of 0.3 day per year and to a minimum elevation angle of 14.4 deg.

a)



b)



c)



d)

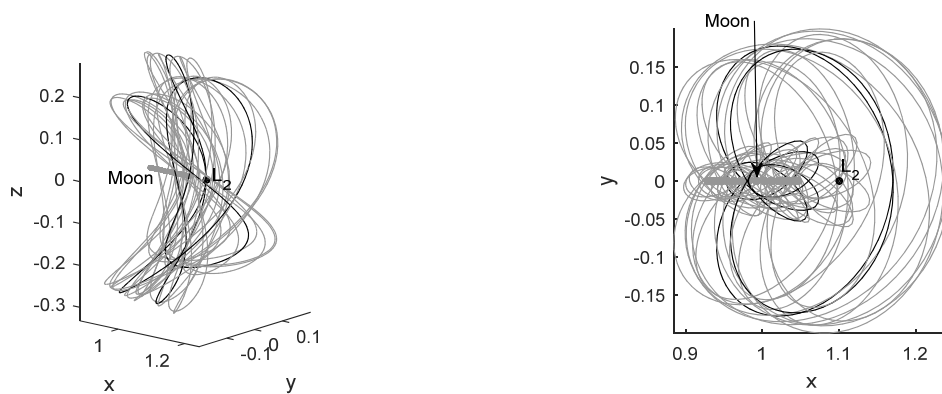


**Figure 17** Perturbed (gray) and unperturbed (black) vertical Lyapunov orbit with  $a_{\theta,EM} = 0.1$  in synodic frame. a) Solar gravity. b) Solar gravity + plane offset. c) Solar gravity + plane offset + eccentricity Earth. d) All perturbations.

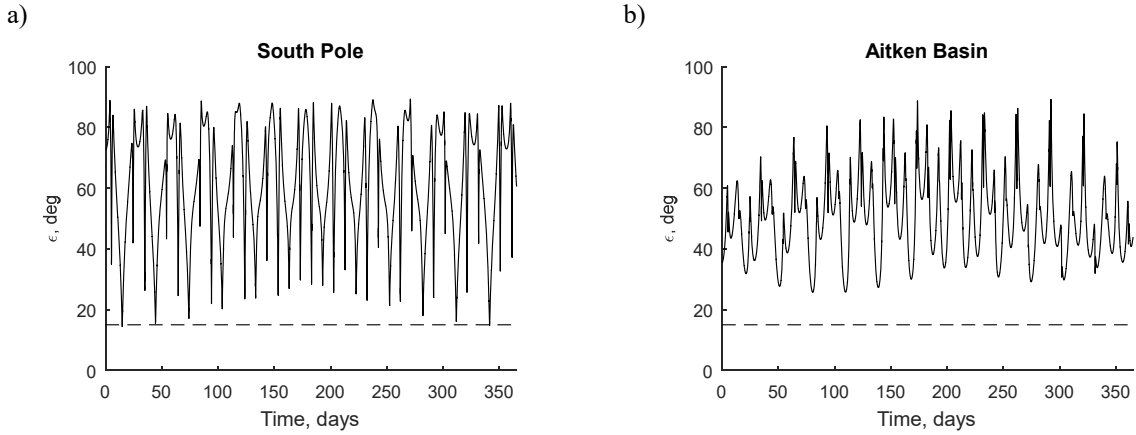


**Figure 18 Elevation at South Pole and Aitken Basin of perturbed constellation of solar sail vertical Lyapunov orbits.**

## Conclusions

A constellation of two clover-shaped orbits has been proposed, modeled in the framework of the circular restricted three-body problem (CR3BP), to achieve near-continuous coverage of the North (or South) Pole (99.6 percent of the time) at a minimum elevation of  $\varepsilon_{\text{lim}} = 27$  deg and continuous coverage of one of the Poles for  $\varepsilon_{\text{lim}} = 20$  deg. An alternative constellation of two clover-shaped orbits achieves 96.3 percent temporal coverage of *both* Poles at  $\varepsilon_{\text{lim}} = 27$  deg (97.4 percent for  $\varepsilon_{\text{lim}} = 20$  deg). Under higher-fidelity models, that include the solar gravity, the offset between the ecliptic and Earth-Moon planes as well as the Earth's and lunar eccentricities, perturbed trajectories are obtained that remain close to the nominal CR3BP orbits. It is shown that this quasi-periodic motion only has a very small impact on the observational capabilities of the orbits, showing a difference in the temporal coverage with respect to the orbits in the CR3BP of -1.7 to +0.1 percent, depending on the constellation and latitude considered.

Also a constellation of two  $L_2$  vertical Lyapunov orbits in the Earth-Moon system has been proposed to establish a simultaneous and continuous observation link with the lunar South Pole and the center of the Aitken Basin at  $\varepsilon_{\text{lim}} = 15$  deg. Due to the closer proximity to the Moon, the effect of the lunar eccentricity is much greater than for the clover-shaped orbits, showing a greater offset between the orbits in the CR3BP and higher-fidelity dynamics. While the center of the Aitken Basin is still continuously in view with elevation angles above the minimum required value of 15 deg, the elevation of the sailcraft at the South Pole drops to a minimum value of 14.4 deg for a total of 0.3 day per year.

Important to note is that both the unperturbed and perturbed orbits have not been optimized for coverage.

Rather than allowing the periodic orbits in the CR3BP to become quasi-periodic under the influence of perturbations, future work will investigate the possibility of orbital control, to track the nominal CR3BP orbits under the influence of the perturbations to maintain the coverage capabilities of the unperturbed orbits.

### Acknowledgements

Jeannette Heiligers would like to acknowledge the support of the Marie Skłodowska-Curie Individual Fellowship 658645 - S4ILS: Solar Sailing for Space Situational Awareness in the Lunar System.

### References

1. McNutt, L., Johnson, L., Clardy, D., Castillo-Rogez, J., Frick, A., and Jones, L., "Near-Earth Asteroid Scout," *AIAA SPACE 2014 Conference and Exposition*, American Institute of Aeronautics and Astronautics, San Diego, CA, 2014.
2. McInnes, C.R., "Solar Sailing: Technology, Dynamics and Mission Applications," *Springer-Praxis Books in Astronautical Engineering*, Springer-Verlag, Berlin, 1999.
3. Vulpetti, G., Johnson, L., and Matloff, G.L., "Solar Sails A Novel Approach to Interplanetary Travel, 2nd Edition," *Springer-Praxis Books in Space Exploration*, 2nd ed., Springer Science+Business Media, New York, 2015.
4. Macdonald, M., McInnes, C., Alexander, D., and Sandman, A., "GeoSail: Exploring the Magnetosphere Using a Low-cost Solar Sail," *Acta Astronautica*; Vol. 59, 2006, pp. 757-767. doi: 10.1016/j.actaastro.2005.07.023
5. Macdonald, M. and McInnes, C., "Solar Sail Science Mission Applications and Advancement," *Advances in Space Research*; Vol. 48, No. 11, 2011, pp. 1702-1716. doi: 10.1016/j.asr.2011.03.018
6. McInnes, C.R., Macdonald, M., Angelopolous, V., and Alexander, D., "GEOSAIL: Exploring the Geomagnetic Tail Using a Small Solar Sail," *Journal of Spacecraft and Rockets*; Vol. 38, No. 4, 2001, pp. 622-629. doi: 10.2514/2.3727
7. Macdonald, M., Hughes, G., McInnes, C., A, L., Falkner, P., and Atzei, A., "GeoSail: An Elegant Solar Sail Demonstration Mission," *Journal of Spacecraft and Rockets*; Vol. 44, No. 4, 2007, pp. 784-796. doi: 10.2514/1.22867
8. West, J.L., "The GeoStorm Warning Mission: Enhanced Opportunities Based on New Technology," *14th AAS/AIAA Spaceflight Mechanics Conference*, AAS-04-102, Maui, Hawaii, 2004.
9. Heiligers, J., Diedrich, B., Derbes, B., and McInnes, C.R., "Sunjammer: Preliminary End-to-End Mission Design," *2014 AIAA/AAS Astrodynamics Specialist Conference*, San Diego, CA, USA, 2014.
10. Macdonald, M., Hughes, G.W., McInnes, C.R., Lyngvi, A., Falkner, P., and Atzei, A., "A Solar Sail Technology Reference Study," *Journal of Spacecraft and Rockets*; Vol. 43, 2006, pp. 960-972
11. Macdonald, M., McInnes, C., and Hughes, G., "Technology Requirements of Exploration Beyond Neptune by Solar Sail Propulsion," *Journal of Spacecraft and Rockets*; Vol. 47, No. 3, 2010, pp. 472-483. doi: 10.2514/1.46657
12. Gautier, D.L., Bird, K.J., Charpentier, R.R., Grantz, A., Houseknecht, D.W., Klett, T.R., Moore, T.E., Pitman, J.K., Schenk, C.J., Schuenemeyer, J.H., Sørensen, K., Tennyson, M.E., Valin, Z.C., and C.J., W., "Assessment of Undiscovered Oil and Gas in the Arctic," *Science*; Vol. 324, No. 5931, 2009, pp. 1175-1179. doi: 10.1126/science.1169467
13. Fear, R.C., Milan, S.E., Carter, J.A., and Maggiolo, R., "The interaction between transpolar arcs and cusp spots," *Geophysical Research Letters*; Vol. 42, No. 22, 2015, pp. 9685-9693. doi: 10.1002/2015GL066194
14. Heiligers, J., Hiddink, S., Noomen, R., and McInnes, C.R., "Solar Sail Lyapunov and Halo Orbits in the Earth-Moon Three-Body Problem," *Acta Astronautica*; Vol. 116, 2015, pp. 25-35. doi: 10.1016/j.actaastro.2015.05.034
15. Heiligers, J., Macdonald, M., and Parker, J.S., "Extension of Earth-Moon Libration Point Orbits with Solar Sail Propulsion," *Astrophysics and Space Sciences, In Press*; Vol. 361 : 241, 2016. doi: 10.1007/s10509-016-2783-3

16. Battin, R.H., "An Introduction to the Mathematics and Methods of Astrodynamics, Revised Edition," *AIAA Education Series*, American Institute of Aeronautics and Astronautics, Inc., Reston, USA, 1999.
17. Howell, K.C., "Three-dimensional, periodic, 'Halo' orbits," *Celestial Mechanics*; Vol. 32, 1983, pp. 53-71. doi: 10.1007/BF01358403
18. Anderson, P. and Macdonald, M., "Extension of Highly Elliptical Earth Orbits Using Continuous Low-Thrust Propulsion," *Journal of Guidance, Control, and Dynamics*; Vol. 36, No. 1, 2013, pp. 282-292. doi: 10.2514/1.55304
19. Ceriotti, M., Heiligers, J., and McInnes, C.R., "Trajectory and Spacecraft Design for a Pole-Sitter Mission," *Journal of Spacecraft and Rockets*; Vol. 51, No. 1, 2014, pp. 311-326. doi: 10.2514/1.A32477
20. Waters, T.J. and McInnes, C.R., "Periodic Orbits Above the Ecliptic in the Solar-Sail Restricted Three-Body Problem," *Journal of Guidance, Control, and Dynamics*; Vol. 30, No. 3, 2007, pp. 687-693. doi: 10.2514/1.26232
21. Ceriotti, M. and McInnes, C., "Natural and sail-displaced doubly-symmetric Lagrange point orbits for polar coverage," *Celestial Mechanics and Dynamical Astronomy*; Vol., 2012. doi: 10.1007/s10569-012-9422-2
22. Milan, S., "KuaFu: Exploring the Sun-Earth Connection," *Astronomy & Geophysics*; Vol. 53, No. 4, 2012, pp. 4.21-4.24. doi: 10.1111/j.1468-4004.2012.53421.x
23. Garand, L. and Morri, T., "Polar Communications and Weather (PCW) Mission - User Requirements Document, Version 6.1," 2011.
24. National Aeronautics and Space Administration (NASA), "NASA's Exploration Systems Architecture Study (NASA-TM-2005-214062)," 2005.
25. Farquhar, R.W., "The Utilization of Halo Orbits in Advanced Lunar Operations, NASA TN D-6365," Washington, D.C., 1971.
26. Farquhar, R.W., "A Halo-Orbit Lunar Station," *Astronautics & Aeronautics*; Vol., 1972, pp. 59-63
27. Grebow, D.J., Ozimek, M.T., and Howell, K.C., "Multibody Orbit Architectures for Lunar South Pole Coverage," *Journal of Spacecraft and Rockets*; Vol. 45, No. 2, 2008, pp. 344-358. doi: 10.2514/1.28738
28. Ozimek, M., Grebow, D., and Howell, K., *Solar Sails and Lunar South Pole Coverage*, in *AIAA/AAS Astrodynamics Specialist Conference and Exhibit*. 2008, American Institute of Aeronautics and Astronautics.
29. Ozimek, M.T., Grebow, D.J., and Howell, K.C., "Design of Solar Sail Trajectories with Applications to Lunar South Pole Coverage," *Journal of Guidance, Control, and Dynamics*; Vol. 32, No. 6, 2009, pp. 1884-1897. doi: 10.2514/1.41963
30. Wawrzyniak, G.G. and Howell, K.C., "Investigating the Design Space for Solar Sail Trajectories in the Earth-Moon System," *The Open Aerospace Engineering Journal*; Vol. 4, 2011, pp. 26-44
31. Wawrzyniak, G.G. and Howell, K.C., "Generating Solar Sail Trajectories in the Earth-Moon System Using Augmented Finite-Difference Methods (Article ID 476197)," *International Journal of Aerospace Engineering*; Vol., 2011. doi: 10.1155/2011/476197
32. Biggs, J.D., McInnes, C.R., and Waters, T., "Control of Solar Sail Periodic Orbits in the Elliptic Three-Body Problem," *Journal of Guidance, Control, and Dynamics*; Vol. 32, No. 1, 2009, pp. 318-320. doi: 10.2514/1.38362
33. Wertz, J.R., "Mission Geometry; Orbit and Constellation Design and Management," Space Technology Library, Microcosm Press/Kluwer Academic Publishers, El Segundo, USA/London, UK, 2001.
34. Parker, J.S. and Anderson, R.L., "Low-Energy Lunar Trajectory Design," *Deep Space Communications and Navigation Series*, Jet Propulsion Laboratory, Pasadena, California, USA, 2013.
35. Howell, K.C. and Pernicka, H.J., "Numerical Determination of Lissajous Trajectories in the Restricted Three-Body Problem," *Celestial Mechanics*; Vol. 41, 1988, pp. 107-124
36. Marchand, B.G., Howell, K.C., and Wilson, R.S., "Improved Corrections Process for Constrained Trajectory Design in the n-Body Problem," *Journal of Spacecraft and Rockets*; Vol. 44, No. 4, 2007, pp. 884-897